Glia detect and transiently protect against dendrite substructure disruption in *C. elegans*

Katherine C. Varandas [1], Brianna M. Hodges[1], Lauren Lubeck [1,3], Amelia Farinas[1,4], Yupu Liang[2,5], Yun Lu[1] & Shai Shaham [1] ✉

Glia assess axon structure to modulate myelination and axon repair. Whether glia similarly detect dendrites and their substructures is not well understood. Here we show that glia monitor the integrity of dendrite substructures and transiently protect them against perturbations. We demonstrate that disruption of *C. elegans* sensory neuron dendrite cilia elicits acute glial responses, including increased accumulation of glia-derived extracellular matrix around cilia, changes in gene expression, and alteration of secreted protein repertoire. DGS-1, a 7-transmembrane domain neuronal protein, and FIG-1, a multifunctional thrombospondin-domain glial protein, are required for glial detection of cilia integrity, physically interact, and exhibit mutually-dependent localization to and around cilia, respectively. Glial responses to dendrite cilia disruption transiently protect against damage. Thus, our studies uncover a homeostatic, protective, dendrite-glia signaling interaction regulating dendrite substructure integrity.

The elaborate structures of neurons determine connectivity and functional output in the nervous system. Neurons typically extend axons and dendrites, polarized projections that mediate signal transmission and reception, respectively[1]. Many axons are ensheathed by glia, as are dendritic substructures[2]. For example, dendritic spines, which mediate reception of presynaptically-released neurotransmitters[3], are often surrounded by astrocyte processes[4], and microtubule-rich cilia at dendritic endings of sensory neurons are also enveloped by adjacent glia[5].

Glia are major players in neurological injury and disease, with diverse roles in causing, protecting from, and contributing to loss of neuron function[6]. While glia surrounding axons are known to detect axon diameter for proportional myelination[7] and respond to axon damage to promote or block regeneration or repair[8], glial responses to dendrite structural changes are less understood. Yet, changes in dendritic substructures are commonplace during learning and memory formation and are a hallmark of nervous system diseases[9]. For example, ciliopathies, genetic disorders leading to abnormal cilia structure or function, often cause profound sensory deficits[10]. We set out, therefore, to determine whether glia can monitor and respond to changes in dendrite structure.

The sensory organs of *C. elegans* are excellent settings to study dendrite-glia communication, as their anatomy, cellular makeup, and molecular components are conserved in insects and mammals[11–13]. Most *C. elegans* glia physically associate with neuronal dendritic endings in sensory organs[14] and these interactions are generally anatomically invariant[15–17]. Since cilia are only found at sensory dendrite endings in *C. elegans*[18], cilia mutants can be used to specifically model the effects of dendrite substructure disruption on neighboring glia.

The amphids are a pair of bilaterally-symmetric head sensory organs, each containing twelve sensory neurons, of which eight extend anterior dendrites ending in simple cilia housing sensory receptors and signal transduction machinery (Fig. 1a)[15]. These cilia

[1]Laboratory of Developmental Genetics, The Rockefeller University, New York, NY, USA. [2]CCTS Research Bioinformatics, The Rockefeller University, New York, NY, USA. [3]Present address: Graduate Program in Biology, Hopkins Marine Station of Stanford University, Pacific Grove, CA, USA. [4]Present address: Graduate Program in Neuroscience, Stanford University, Stanford, CA, USA. [5]Present address: Bioinformatics Data Engineering, Alexion Pharmaceuticals, Boston, MA, USA. ✉e-mail: shaham@rockefeller.edu
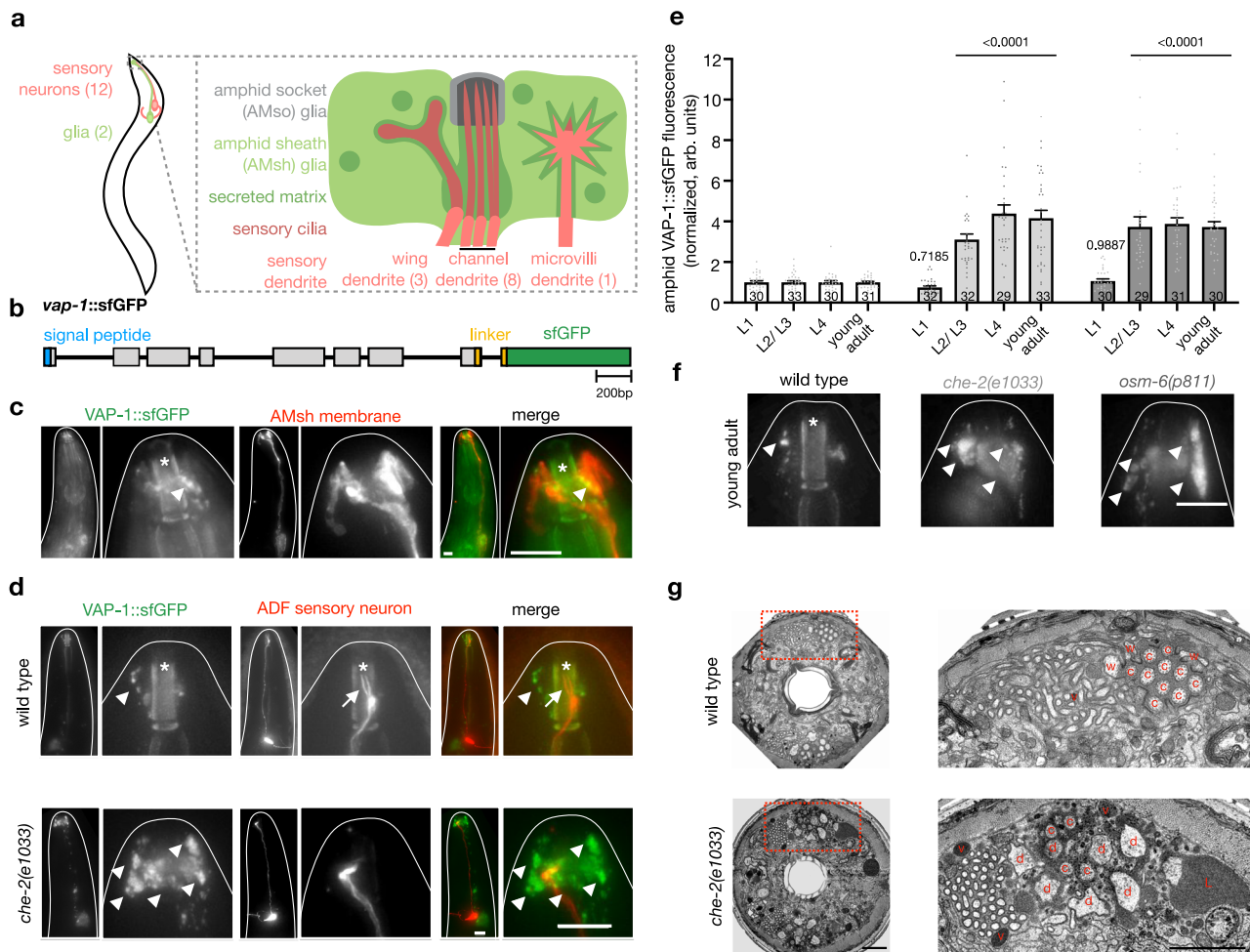
Fig. 1 | AMsh glia modify their secretory activity in dendrite cilia mutants.
a Schematic of an amphid sensory organ. **b** CRISPR edited *vap-1::sfGFP* locus. **c** *vap-1::sfGFP* animal expressing AMsh glia membrane reporter (*F16F9.3pro::myr-mKate2*). GFP channel is background subtracted. Arrowheads, VAP-1::sfGFP accumulation. Asterisk, anterior buccal cavity auto-fluorescence. Scale bar = 10 µm. **d** Brightness and contrast-matched images of wild type and *che-2(e1033)* animals co-expressing *vap-1::sfGFP* and a reporter for the ADF channel sensory neuron (*srh-142pro::dsRed*), which extends two sensory cilia into the amphid channel. Arrows, dendrite cilia. Arrowheads, VAP-1::sfGFP puncta. Asterisk, anterior buccal cavity auto-fluorescence. Scale bars = 10 µm. **e** Quantification of amphid VAP-1::sfGFP fluorescence in wild-type, *che-2(e1033)*, and *osm-6(p811)* animals at 24 h intervals over larval development, normalized to wild type at the same timepoint. Data are presented as mean + SEM. *n*, indicated inside bars, represents the number of individual animals quantified from 3 independent experiments. Adjusted *P* values in comparison to wild type at the same timepoint calculated using Dunnett's multiple comparison test following ordinary two-way ANOVA. **f** Brightness and contrast matched images of VAP-1::sfGFP in young adult animals of indicated genotypes, representative of images analyzed in **e**. Arrowheads, asterisk, as in **c**. Scale bar = 10 µm. **g** Full TEM cross sections (left) and insets (right) of wild type and *che-2(e1033)* mutant animals. c, channel cilia. w, wing cilia. d, dendrite. L, amphid channel lobe. v, matrix-filled AMsh vesicle. Scale bars=2µm. All fluorescence images are maximum intensity projections of widefield z-stacks. Source data are provided as a Source Data file.

are required for sensory neuron function[19] and protrude through a channel formed by two glial cells: the amphid sheath (AMsh) glial cell, which secretes an extracellular matrix around the cilia, and the amphid socket (AMso) glial cell, which forms a pore through which cilia are exposed to the environment[15,20]. Four other amphid neurons have modified ciliary dendritic endings that are ensheathed only by AMsh glia: three with elaborately-structured wing cilia, and another with an actin-rich microvilli dendrite ending[21,22].

Here we report that AMsh glia actively monitor the structural integrity of sensory dendrite cilia and elicit responses that protectively delay dendrite cilia damage. In mutants with defective cilia, AMsh glia secrete excess matrix around dendrite endings and accumulate matrix-laden secretory vesicles. These changes in secretion are accompanied by transcriptional changes in AMsh glia that alter its secretory protein repertoire and correlate with increased activity of the conserved glial transcription factor PROS-

1/Prox1. By inducibly disrupting cilia, we show that the glial secretory response is acute. We identify two proteins, DGS-1 and FIG-1, that mediate glial detection of and responses to cilia changes. DGS-1 is an uncharacterized 7-transmembrane domain protein expressed in a subset of amphid sensory neurons and localized to dendrite cilia. FIG-1 is a transmembrane thrombospondin domain-containing protein expressed in AMsh glia and localized around amphid channel cilia. DGS-1 and FIG-1 physically interact and their protein localization is mutually dependent. In either *dgs-1* or *fig-1* mutants, cilia are intact, yet AMsh glia exhibit secretory changes similar to those seen in mutants with abnormal cilia structure. Mutation of *dgs-1* or *fig-1* delays the onset of cilia dysfunction following inducible cilia disruption, demonstrating that the glial responses are protective. Our studies reveal the importance of glia in monitoring and maintaining homeostasis of dendritic signaling compartments in the nervous system.

Results

AMsh glia modify their secretory activity in dendrite cilia mutants

AMsh glia express many secreted proteins, some of which are components of a specialized extracellular matrix surrounding sensory-neuron dendritic cilia[23]. We wondered, therefore, whether disrupting dendrite cilia might affect secretion from AMsh glia. To test this, we used CRISPR/Cas9 to fuse the endogenous *vap-1* gene, encoding an AMsh glia-enriched secreted protein[23], to coding sequences for superfolder GFP (sfGFP), optimized for fluorescence in the extracellular milieu (Fig. 1b)[24]. In these animals, VAP-1::sfGFP localizes to the anterior region of AMsh glia and is found in discreet puncta, as expected for a protein packaged into vesicles and secreted around sensory cilia (Fig. 1c, d top panel).

We next examined VAP-1::sfGFP in *che-2(e1033)* mutant animals, which have truncated cilia[22,25]. *che-2* encodes a homolog of the IFT80 subunit of the ciliary intraflagellar transport B (IFT-B) complex and is expressed exclusively in ciliated sensory neurons in *C. elegans*[18,25]. We observed a marked increase in VAP-1::sfGFP accumulation around amphid sensory cilia in these mutants (Fig. 1d, compare top and bottom panels). Similar accumulation is evident in loss-of-function mutants of the ciliary rootlet gene *che-10*/rootletin, the IFT-A complex gene *che-11*/IFT140, and the IFT-B complex genes *osm-5*/IFT88, *osm-6*/IFT52, and *dyf-11*/IFT54 (Supplementary Fig. 1a, b), all of which exhibit truncated cilia[25–27]. Imaging wild-type, *che-2(e1033)*, and *osm-6(p811)* animals at 24-h intervals over larval development revealed that in both mutants, excess VAP-1::sfGFP accumulation is first detectable in L2/L3 larvae and persists into adulthood (Fig. 1e, f). To determine if these changes are due to increased expression of *vap-1*, we examined mRNA levels and transcriptional reporters. While we did not observe significant changes in *vap-1* mRNA levels (Supplementary Fig. 1c, d), expression of a *vap-1* transcriptional reporter was increased more than 2 fold in the AMsh glia of *che-2(e1033)* mutants compared to wild type (Supplementary Fig. 1e). These results suggest that *vap-1* expression is increased, however given the caveats associated with transcriptional reporters, the observation would require further verification.

To confirm secreted matrix accumulation in cilia mutants, we examined amphid ultrastructure in wild-type and *che-2(e1033)* mutant animals using serial-section transmission electron microscopy (TEM; 2 amphids/strain). In *che-2(e1033)* mutants, we observed excess extracellular matrix in lobe-like outpockets herniating from the AMsh glia channel. Within AMsh glia, excess matrix-laden vesicle accumulation was evident (Fig. 1g, compare top and bottom panels). These observations are consistent with our VAP-1::sfGFP findings and previous TEM studies suggesting that AMsh glia accumulate vesicles containing extracellular matrix in cilia mutants[22,28].

Taken together, our data demonstrate that AMsh glia detect the loss of dendrite cilia integrity and respond by increasing the number of extracellular matrix-laden vesicles around the glial channel housing these cilia and by accumulating excess extracellular matrix in this channel.

AMsh glia transcription is altered in dendrite cilia mutants, correlating with increased PROS-1/Prox1 activity

To further explore how loss of cilia integrity affects AMsh glia, we performed RNA sequencing (RNA-seq) on cells isolated from late-stage wild-type or *che-2(e1033)* larvae expressing an AMsh glia-specific reporter (*F16F9.3*pro::dsRed). AMsh glia (dsRed +) from each strain were sorted from all other cells (dsRed-) using fluorescence activated cell sorting (FACS)[23]. Comparison of AMsh glia transcripts expressed in dsRed+ and dsRed- cells, from either wild-type or *che-2* animals, shows enrichment of mRNAs previously described as AMsh glia-enriched, validating our cell isolation and RNA-seq methodologies (Supplementary Fig. 2a, b)[23,29]. This finding also demonstrates that AMsh glia

cell fate is not entirely altered in cilia mutants, as these AMsh glia-enriched genes are expressed to a similar degree in wild-type and *che-2(e1033)* animals. Nonetheless, we identified several hundred genes whose expression is either increased (673 genes; FC ≥ 2, padj ≤ 0.1, Supplementary Data 1) or decreased (485 genes; FC ≤ 0.5, padj ≤ 0.1, Supplementary Data 2) in AMsh glia of *che-2* cilia mutants (Supplementary Fig. 2c). This finding was further confirmed in animals carrying reporter transgene fusions to differentially-expressed gene regulatory sequences (Supplementary Fig. 2d).

Of genes with increased expression in *che-2* mutants, 28% (185/673) are predicted to encode membrane proteins and 4% (24/673) are predicted to encode secreted proteins. Of the downregulated genes, 33% (159/485) are predicted to encode membrane proteins and 6% (30/485) are predicted to encode secreted proteins (Supplementary Data 1 and 2). Thus, in addition to accumulating secreted matrix, glia respond to defects in dendrite cilia by altering expression of over 1000 genes, many of which encode proteins predicted to enter the secretory pathway.

PROS-1, a major transcriptional regulator of the AMsh glia secretome[23,30], is homologous to *Drosophila* Prospero and to mammalian Prox1, both of which are also expressed in sensory organ glia[23,31–33]. Consistent with the idea that the secretory pathway in AMsh glia is altered upon cilia disruption, genes whose expression is induced or repressed by PROS-1 cluster more than expected statistically with genes up-regulated or down-regulated in AMsh glia of *che-2(e1033)* mutants, respectively (Supplementary Fig. 2e). PROS-1-induced genes are, on average, more enriched in AMsh glia of *che-2(e1033)* mutants than PROS-1-repressed genes (Supplementary Fig. 2f). Likewise, expression of *vap-1*, which is increased in AMsh glia in cilia mutants compared to wild type (Supplementary Fig. 1e), is PROS-1 induced[23]. These data suggest that the transcriptional response of AMsh glia to cilia defects may result from increased activation of PROS-1, which controls the secretory repertoire of AMsh glia.

Expression of a PROS-1::GFP reporter is not increased in AMsh glia of cilia mutants and *pros-1* mRNA levels are similarly unaffected (Supplementary Fig. 2g, h). Therefore, in addition to transcriptional changes, post-transcriptional changes affecting the secretory pathway must also occur in AMsh glia in response to cilia disruption.

The AMsh glia response to cilia disruption is acute

Animals carrying mutations in *che-2*, *osm-6*, or other cilia genes have chronic cilia defects, which can be monitored by assaying the ability of a subset of ciliated neurons to take up the small-molecule dyes DiI or DiO[19]. To determine whether the glial response to cilia defects also follows acute cilia perturbation, we designed an inducible cilia disruption system. Briefly, sequences encoding AID, an auxin-inducible degron[34,35], were introduced into the genomic *osm-6* locus of animals also ubiquitously expressing the AID-targeting scaffold protein TIR1 (*eft-3pro::TIR1-mRuby*; Fig. 2a; a related method is described in ref. 36). While control animals containing either *osm-6::AID* or *eft-3pro::TIR1-mRuby*, have no dye-filling defects, in the majority of animals containing both, sensory neurons become dye-filling defective within 1.5 h of auxin exposure (Fig. 2b). TEM micrographs of a dye-filling defective animal reveal cilia damage, as expected (Supplementary Fig. 3; 2 amphids observed). Furthermore, in animals in which OSM-6 protein is tagged with both GFP and AID, GFP fluorescence loss following auxin exposure is evident (Fig. 2c), confirming OSM-6 protein degradation.

We next used our inducible cilia degradation system to assess AMsh glia response dynamics following acute cilia disruption. We exposed developmentally-synchronized *vap-1::sfGFP; osm-6::AID; eft-3pro::TIR1-mRuby* animals to auxin at different times prior to imaging as young adults and found that VAP-1::sfGFP progressively accumulates at the AMsh glia tip (Fig. 2d, e). Control animals carrying only *osm-6::AID* or *eft-3pro::TIR1-mRuby*, show no VAP-1::sfGFP accumulation
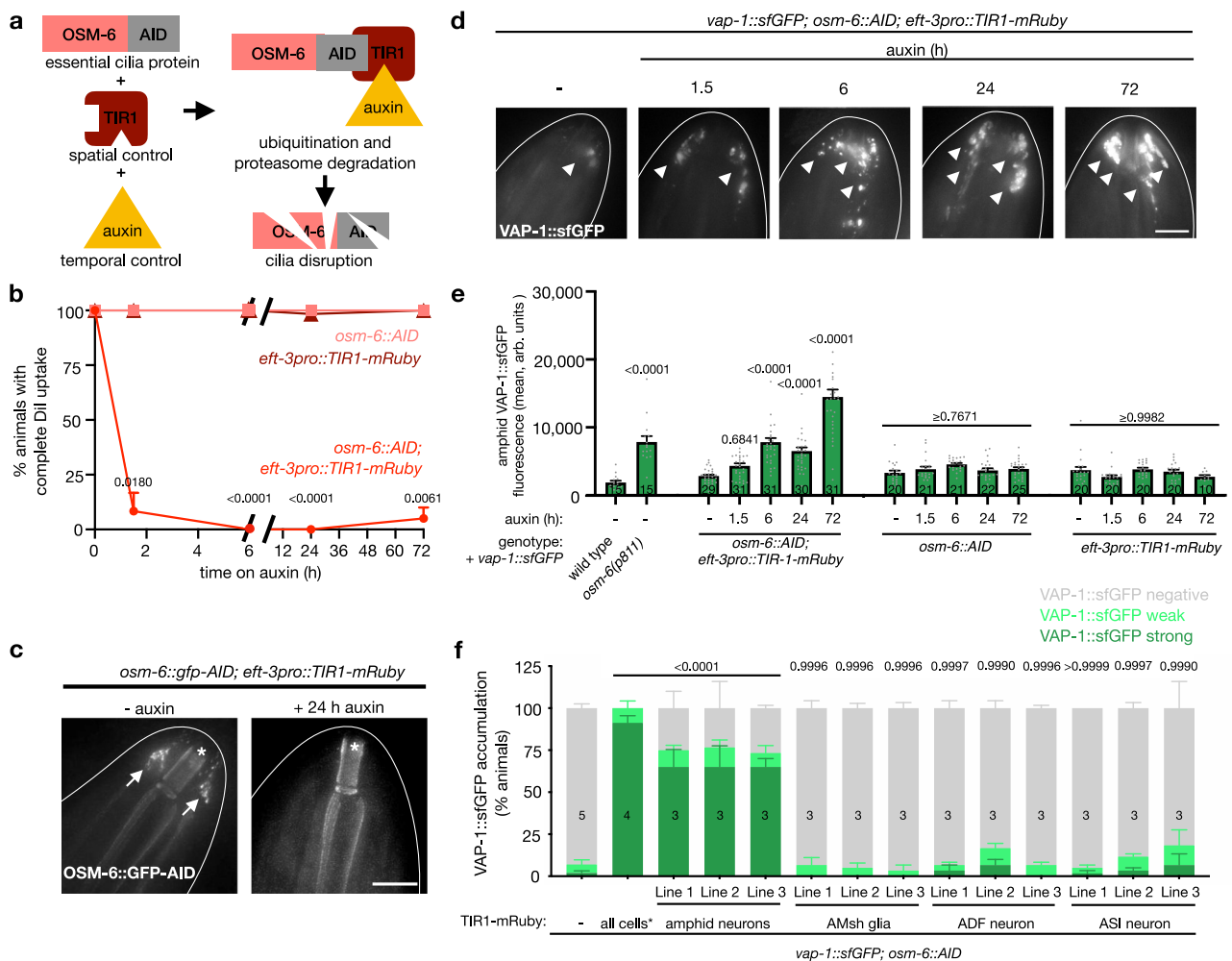
Fig. 2 | The AMsh glia response to cilia disruption is acute. a Strategy for inducible cilia disruption. **b** Amphid dye-filling time course of animals with indicated inducible cilia disruption components. *n* = 3 trials, 20 animals scored/ timepoint/ trial. Adjusted *P* values in reference to same genotype 0 h auxin, calculated using Dunnett's multiple comparison test following two-way repeated measures ANOVA, reported if *P* < 0.05. **c** Brightness and contrast-matched images of *osm-6::gfp-AID* in animals ubiquitously expressing TIR1-mRuby (*eft-3pro::TIR1-mRuby*) without auxin or following 24 h of auxin treatment. Arrows, OSM-6::GFP-AID in amphid. Asterisks, anterior buccal cavity auto-fluorescence.
d Representative brightness and contrast-matched images of VAP-1::sfGFP in *osm-6::AID* animals also ubiquitously expressing TIR1-mRuby (*eft-3pro::TIR1-mRuby*) without auxin or treated with auxin for indicated time. Arrowheads, VAP-1::sfGFP puncta. **e** Quantification of VAP-1::sfGFP accumulation in the amphids of animals with indicated genotypes and auxin treatment time. *n*, indicated inside bars, represents the number of animals quantified. Adjusted *P* values in relation to -

auxin of the same genotype, or wild type condition for *osm-6(p811)*, calculated using Sidak's multiple comparison test following one-way ANOVA reported. Adjusted *P* values not reported in figure: *osm-6::AID*: 1.5 h = 0.9998, 6 h = 0.7671, 24 h > 0.9999, 72 h = 0.9993; *eft-3pro::TIR1-mRuby*: 1.5 h = 0.9545, 6 h = >0.9999, 24 h = 0.9999, 72 h = 0.9928. **f** VAP-1::sfGFP accumulation in *osm-6::AID* animals exposed to auxin for 72 h expressing TIR1-mRuby in indicated cell types. *n*, indicated inside bars, represents number of trials scored, 20 animals/ trial. Adjusted *P* values in relation to - TIR1-mRuby calculated from % animals with strong VAP-1::sfGFP accumulation with Dunnett's multiple comparison test following one-way ANOVA. *TIR1-mRuby is expressed in all cells (*eft-3pro::TIR1-mRuby*) from a genetically integrated transgene, while cell-specific TIR1-mRuby is expressed from extrachromosomal arrays. Images are maximum intensity projections of widefield z-stacks. Auxin treatments at 4 mM. Scale bars = 10 μm. Data are represented as mean + SEM. Source data are provided as a Source Data file.

(Fig. 2e). We conclude that AMsh glia respond within hours to disruption of dendrite cilia.

To determine whether cilia disruption of multiple channel neurons is required to elicit a glial response, we constructed *vap-1::sfGFP; osm-6::AID* animals that express TIR1-mRuby only in specific cells or cell combinations. When TIR1-mRuby is expressed in all amphid neurons, glial VAP-1::sfGFP accumulates in most animals exposed to auxin for 72 h. Animals in which TIR1-mRuby is expressed in AMsh glia show no accumulation (Fig. 2f), as expected. Disruption of cilia in the individual channel neurons ADF or ASI results in VAP-1::sfGFP accumulation in only a few animals (Fig. 2f). Thus, AMsh glia require disruption of multiple dendrite cilia to elicit the full matrix accumulation response.

Mutants in DGS-1, a 7-transmembrane domain protein, have intact cilia yet aberrantly accumulate glia-secreted matrix

To identify genes involved in signaling dendrite cilia loss to AMsh glia, we mutagenized *vap-1::sfGFP* animals also expressing an amphid neuron reporter, and screened F2 progeny for mutants that accumulate VAP-1::sfGFP at AMsh glia tips. To exclude mutants with cilia structural defects, only candidates with normal cilia morphology, assessed using an ADF sensory neuron reporter, and whose amphid neurons uptake DiI were further studied. From this screen, we isolated a homozygous mutant, *ns942*, in which VAP-1::sfGFP accumulation is pronounced (Fig. 3a) despite normal amphid dye uptake (Supplementary Fig. 4a, b).

Using whole genome sequencing, single-nucleotide polymorphism mapping, and transformation rescue, we demonstrated
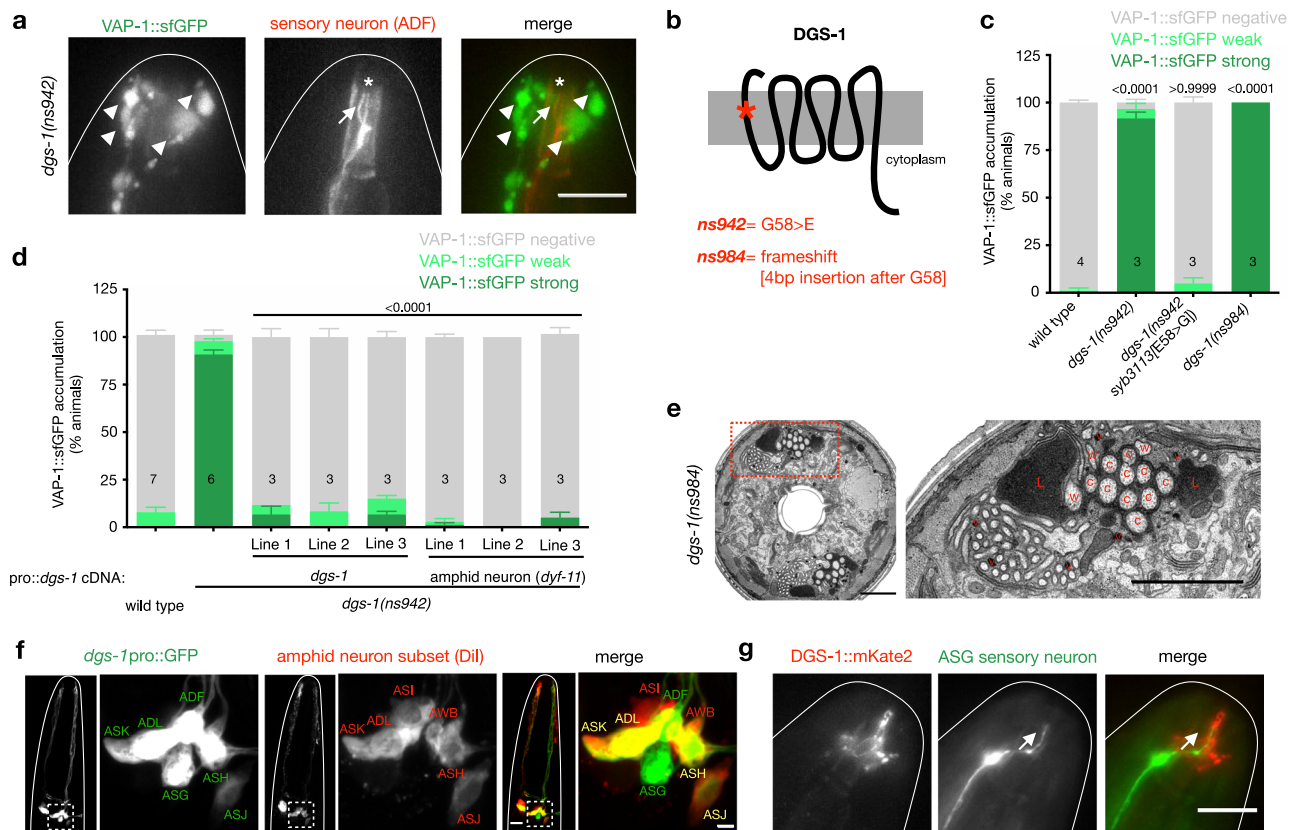
Fig. 3 | Mutants in *dgs-1*, which encodes a cilia-localized 7-transmembrane domain protein, have intact cilia yet aberrantly accumulate glia-secreted matrix. a Widefield images of a *dgs-1(ns942)*; *vap-1::sfGFP* animal expressing an ADF neuron reporter (*srh-142*pro::dsRed). Images representative of *n* = 30 animals from 3 biological replicates quantified in panel **c**. VAP-1::sfGFP images are brightness and contrast-matched to Fig. 1d for comparison. Arrow, dendrite cilia. Arrowheads, VAP-1::sfGFP accumulation. Asterisk, anterior buccal cavity auto-fluorescence. Scale bar = 10 μm. **b** DGS-1 predicted topology and mutations analyzed. **c** VAP-1::sfGFP accumulation in animals of indicated genotype. Adjusted *P* values in relation to wild type. **d** VAP-1::sfGFP accumulation in animals of indicated geno-type. Adjusted *P* values in relation to *dgs-1(ns942)*. **e** Full TEM section through a *dgs-1(ns942)*; *vap-1::sfGFP* animal expressing an ADF neuron reporter

(*srh-142*pro::dsRed; left) and inset (right). c, channel cilia. w, wing cilia. L, amphid channel lobe. v, matrix-filled AMsh vesicle. Scale bars = 2 μm. **f** Confocal images of a *dgs-1*pro::GFP animal labeled with DiI, taken up by a subset of sensory neurons. Left panels, head region. Right panels, inset of neuron cell bodies of one amphid. Scale bars, left = 10 μm, right = 2 μm. **g** Representative wide-field image of an animal expressing DGS-1::mKate2 and ASG neuron reporter (*ops-1*pro::GFP). Scale-bar=10μm. Arrow, dendrite cilia. Fluorescence images are maximum intensity projections of z-stacks. Data are represented as mean + SEM. *n*, indicated inside bars, represents number of trials scored, 20 animals/ trial. Adjusted *P* values cal-culated using Tukey's multiple comparison following ordinary one-way ANOVA of % animals with strong VAP-1::sfGFP accumulation. Source data are provided as a Source Data file.

that *ns942* is a recessive allele with a causal lesion in the previously uncharacterized gene *C09B9.1*, which we renamed dendrite-glia-sig-naling-1 (*dgs-1*). *dgs-1* encodes a predicted 7-transmembrane domain protein conserved among nematode species (Supplementary Fig. 5). *ns942* mutants have a predicted glycine-to-glutamic acid substitution at position 58 in the first transmembrane domain (Fig. 3b). To con-firm that *dgs-1* is the relevant gene, we repaired the *dgs-1(ns942)* lesion (*dgs-1(ns942 syb3113[E58 > G])*) and observed restoration of baseline VAP-1::sfGFP accumulation (Fig. 3c). Furthermore, animals homozygous for a loss-of-function frameshift allele (*ns984*), in which four base pairs are inserted following the G58 codon, also exhibit aberrant VAP-1::sfGFP accumulation (Fig. 3c). Finally, *ns942* mutants expressing a *dgs-1* cDNA using *dgs-1* regulatory sequences (*dgs-1*pro::*dgs-1* cDNA), show near complete rescue of the VAP-1::sfGFP accumulation defect (Fig. 3d).

To determine whether *dgs-1* mutants have ultrastructural changes similar to those of cilia mutants, we examined *dgs-1(ns984)* animals by TEM. While amphid cilia of *dgs-1* mutants appear grossly intact, the amphid channel membrane has lobe-like herniations containing electron-dense secreted matrix material and vesicles filled with electron-dense matrix accumulate in *dgs-1* mutants (Fig. 3e; 6 amphids

observed). Thus, despite having intact cilia, *dgs-1* mutants exhibit AMsh glia secretion responses resembling those of cilia mutants.

DGS-1 functions in dendrite cilia

To determine where DGS-1 functions, we first examined expression of a *dgs-1*pro::GFP reporter transgene. We observed GFP fluorescence in six of eight amphid channel sensory neurons and in neurons of the tail phasmid sensory organ (Fig. 3f and Supplementary Fig. 4c)[19]. We identified four of the neurons that express *dgs-1* as ADL, ASK, ASH, and ASJ by co-labeling with DiI (Fig. 3f). The remaining two neurons, ADF and ASG, were identified by co-labeling with neuron-specific reporters (Supplementary Fig. S4d, e). Supporting these cell assignments, RNA-seq expression data from the CeNGEN database[37] and our experiments show that in the amphid, *dgs-1* transcripts are enriched only in the six neurons we identified and not in other neurons or glia (Supplemen-tary Fig. 4f).

Expression of *dgs-1* cDNA using the *dyf-11* sensory neuron-specific promoter in *dgs-1(ns942)* mutants, results in strong rescue of VAP-1::sfGFP accumulation, supporting a neuronal site-of-action for DGS-1 (Fig. 3d). We also expressed TIR1-mRuby using the *dgs-1* promoter in *vap-1::sfGFP; osm-6::AID* animals. Transgenic animals exposed to auxin

for 72 h display pronounced VAP-1::sfGFP accumulation, comparable to that seen in animals in which cilia of all amphid neurons are disrupted (Supplementary Fig. 4g, compare to Fig. 2f). Thus, perturbing only the neurons in which DGS-1 is expressed is sufficient to elicit the full glial response.

To determine where DGS-1 localizes within sensory neurons, we inserted mKate2 fluorescent protein coding sequences into the predicted third intracellular loop of *dgs-1* (DGS-1::mKate2, Supplementary Fig. 4h). This fusion protein is fully functional, as *dgs-1(ns942)* animals expressing it have no AMsh glia secretory changes (Supplementary Fig. 4i). We find that DGS-1::mKate2 localizes to cilia at the anterior tips of amphid sensory dendrites (Fig. 3g).

Together, our data demonstrate that DGS-1 functions in the cilia of six amphid sensory neurons to signal the presence of intact dendrite cilia to the surrounding AMsh glial cell.

FIG-1, an AMsh glia-expressed protein, functions in glial monitoring of cilia integrity

While DGS-1 functions in neurons to report on dendrite cilia integrity, glial proteins must exist that receive this signal. We found that deleting the gene *fig-1*, encoding two isoforms including a glia-expressed transmembrane protein with a large extracellular domain, results in strong VAP-1::sfGFP accumulation (*fig-1(Δcoding sequence)*; Fig. 4a–c). Like *dgs-1* and *che-2* mutants, serial-section TEM reveals that this mutant has large lobe-like amphid channel herniations containing matrix material and also accumulates matrix-laden glial secretory vesicles near the channel membrane (Fig. 4d; 2 amphids observed). Similar changes are observed for another *fig-1* mutant, *fig-1(tm2079)* (Fig. 4b and Supplementary Fig. 6a; 4 amphids observed). Importantly, sensory neuron cilia appear normal by fluorescent imaging of the ADF sensory neuron reporter and in ultrastructure in *fig-1(Δcoding sequence)* and *fig-1(tm2079)* mutants (Fig. 4c, d and Supplementary Fig. 6a), consistent with previous work showing that neurons are largely functional in animals with *fig-1* inactivation[29].

FIG-1's role in regulating secretion from AMsh glia is distinct from its previously-described function in neuron dye uptake

Previous studies demonstrated that *fig-1(tm2079)* mutants have defects in amphid neuron dye uptake[29], and we observed similar defects in *fig-1(Δcoding sequence)* mutants (Supplementary Fig. 6b). The precise cause of the dye filling defect in these mutants is not known, as loss of dye uptake does not correlate with defects of sensory cilia in *fig-1* mutants (Fig. 4c, d and Supplementary Fig. 6a), suggesting a mechanism by which glia regulate the ability of sensory neurons to uptake these dyes. To determine whether the roles of FIG-1 in regulating secretion from AMsh glia and in neuronal dye filling are related, we performed an in vivo structure-function analysis of *fig-1*. The *fig-1* locus generates two transcripts, predicted to encode proteins of 138 and 2898 amino acids (FIG-1a and FIG-1b, respectively; Fig. 4a). We found that deletion of the *fig-1b* intron containing the first exon of *fig-1a*, *fig-1(Δisoform a)*, has no effect on either VAP-1::sfGFP accumulation or dye uptake (Fig. 4b and Supplementary Fig. 6b). We therefore focused our attention on FIG-1b, which, like DGS-1, is conserved in a subset of nematodes (Supplementary Fig. 7).

FIG-1b contains a short N-terminal intracellular region, a transmembrane domain, and two thrombospondin type I (TSP) domains separated by 17 C6 repeats that constitute the bulk of the protein (Fig. 4a). Like the Δ*coding sequence* mutant, in-frame deletion of the transmembrane domain results in VAP-1::sfGFP accumulation and perturbs dye filling (*fig-1ΔTMD*, amino acids 23-51; Fig. 4b and Supplementary Fig. 6b). Similarly, deletion of the C-terminal 24 amino acids of FIG-1b (*fig-1ΔC-terminus*, amino acids 2,874-2,898), or deletion of several C6 repeats, followed by a frame-shift (*tm2079*, amino acids 2250- 2593 and early stop), results in VAP-1::sfGFP accumulation and perturbs dye filling in only the phasmid sensory organs (Fig. 4b and

Supplementary Fig. 6b), indicating that the C-terminal 24 amino acids of FIG-1b are required for both FIG-1 functions.

Surprisingly, an in-frame deletion spanning all 17 C6 repeats (*fig-1ΔC6*, amino acids 755-2788) results in very minor defects in either VAP-1 accumulation or dye-filling (Fig. 4b and Supplementary Fig. 6b). Furthermore, expression of *fig-1* cDNA lacking the coding region for the C6-repeats under endogenous *fig-1* gene regulatory sequences (*fig-1pro::fig-1ΔC6* cDNA) rescues the VAP-1::sfGFP accumulation defect of *fig-1(Δcoding sequence)* mutants (Fig. 4e), demonstrating that the C6 repeats are largely dispensable for FIG-1b function.

TSP domain-containing proteins are secreted from mammalian glia and function in synaptogenesis[38]. Deletion of the C-terminal TSP domain (*fig-1ΔtspC*, amino acids 2823–2873) causes dye-filling defects in the phasmid tail sensory organ, but has only minor effects on VAP-1::sfGFP accumulation and dye uptake by amphid neurons (Fig. 4b and Supplementary Fig. 6b). Deletion of the N-terminal TSP domain has little effect on dye filling or VAP-1::sfGFP accumulation, and deleting both TSP domains does not enhance the defects beyond those observed in the C-terminal TSP domain mutant (Fig. 4b and Supplementary Fig. 6b). Thus, both TSP domains are dispensable for FIG-1's function in detecting dendrite structure defects.

Importantly, deleting the cytoplasmic N-terminal domain (*fig-1ΔN-terminus*, amino acids 2-22) or the unstructured extracellular domain preceding the C6 repeats (*fig-1Δunstructured*, amino acids 115-754), promotes aberrant VAP-1::sfGFP accumulation, but has only minor effects on dye uptake in the amphid or phasmid (Fig. 4b and Supplementary Fig. 6b). These results suggest that FIG-1b has an undescribed role in regulating matrix accumulation that is both independent and separable from its known role regulating in dye uptake of associated neurons.

FIG-1 functions in AMsh glia to regulate secretion and localizes near sensory neuron cilia

fig-1 expression is highly enriched in AMsh glia[29], suggesting that it likely functions in these cells to regulate their secretory output. Previous studies showed that *fig-1* mutant dye-filling defects can be rescued by expressing FIG-1 in AMsh glia or ectopically in sensory neurons[29], suggesting an extracellular site of action. However, we find that expressing FIG-1b in AMsh glia of *fig-1* mutants, but not ectopically in neurons, rescues VAP-1::accumulation (Fig. 4e). These findings are consistent with our structure-function studies demonstrating distinct FIG-1 activities in glial secretion and dye uptake. Furthermore, these findings suggest that while extracellular regions of FIG-1 are important for control of secretion from AMsh glia (Fig. 4b), specific activity within the glial cell is also critical.

To determine where in AMsh glia FIG-1 is localized, we generated animals in which sfGFP coding sequences are inserted into the endogenous *fig-1* locus just before the stop codon (FIG-1::sfGFP). Since these animals do not exhibit dye-filling defects (Supplementary Fig. 6c), we believe that the FIG-1::sfGFP fusion protein generated is functional. We observed FIG-1::sfGFP expression in AMsh glia, as confirmed by co-expression of the AMsh glia membrane reporter *F16F9.3pro::myr-mKate2* (Fig. 4f, arrows), and localized to the anterior part of these glia surrounding the ciliary base (Fig. 4g, arrows). This distribution is consistent with FIG-1b being a transmembrane protein localized to the amphid channel. We also consistently observed two discreet FIG-1::sfGFP puncta outside of the AMsh glia membrane (Fig. 4f, arrowheads), which are located at the tips of amphid channel dendrite cilia marked by DGS-1::mKate2 (Fig. 4g, arrowheads). Anterior puncta are also seen when FIG-1 is tagged internally (Supplementary Fig. 6d), indicating that these puncta contain FIG-1b and not exclusively FIG-1a. We believe that these puncta are not important for FIG-1 function in glia secretion, however (see below), and that the distinct localization sites of FIG-1b may reflect the different functions of FIG-1 in glial secretion and in neuronal dye uptake.
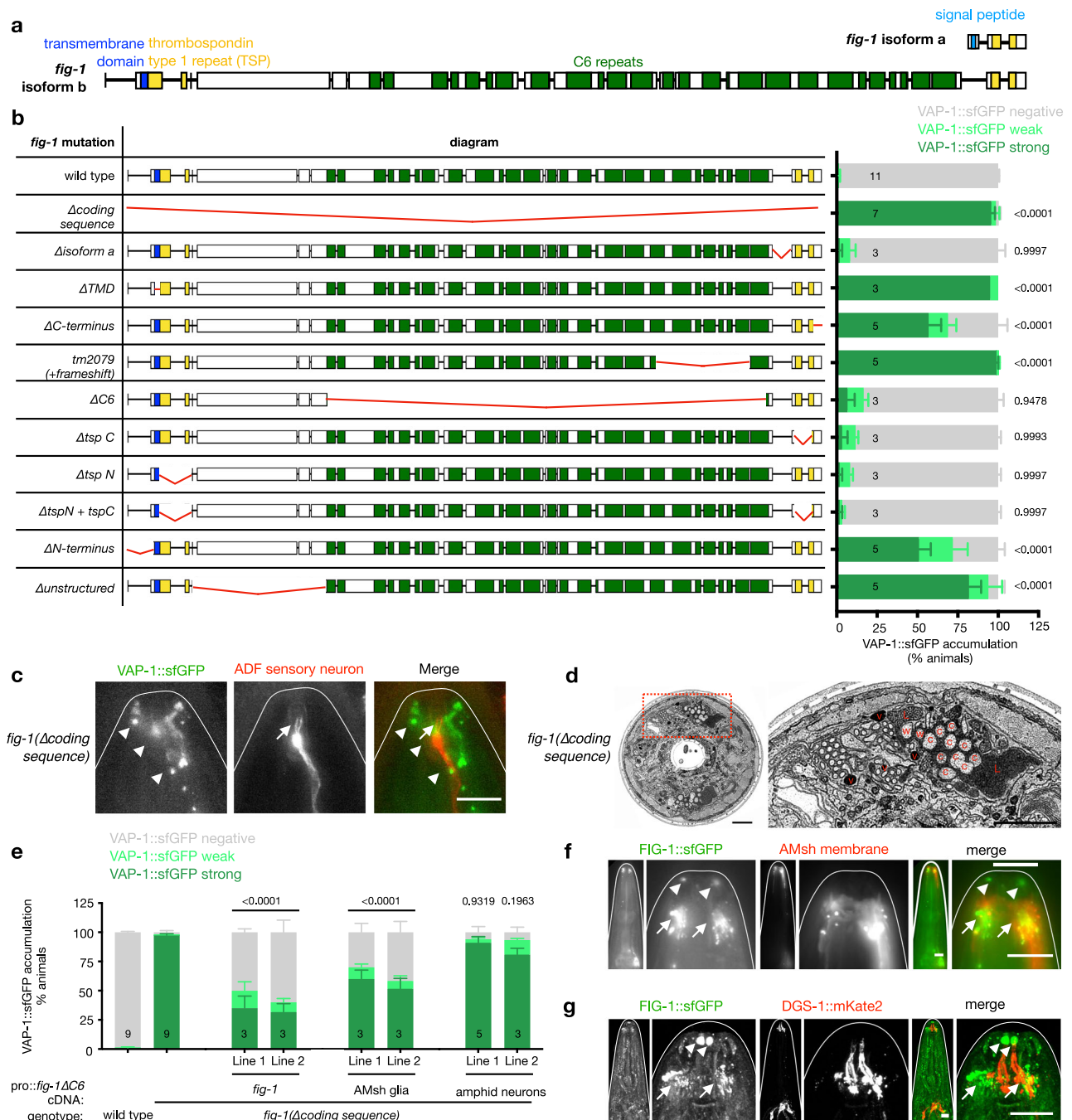
Fig. 4 | FIG-1, an AMsh glia-expressed protein, is required for monitoring cilia integrity. a Predicted *fig-1* gene structure and protein domains. **b** VAP-1::sfGFP accumulation in wild type animals and indicated *fig-1* mutants. *n*, indicated inside bars, represents number of trials scored, 20 animals/ trial. Adjusted *P* values in relation to wild type animals calculated using Dunnett's multiple comparison following one-way ANOVA from % animals with strong VAP-1::sfGFP accumulation reported. **c** Widefield images of *vap-1::sfGFP* animal expressing an ADF neuron reporter (*srh-142pro::dsRed*) in *fig-1*(Δcoding sequence*)* mutant. Arrows, cilia. Arrowheads, VAP-1::sfGFP accumulation. Scale bar = 10 μm. **d** Full TEM cross section of *fig-1*(Δcoding sequence*)* mutant (left), with enlarged inset (right). c, channel cilia. w, wing cilia. L, amphid channel lobes. V, matrix-filled AMsh vesicle. Scale bars = 2 μm. **e** VAP-1::sfGFP accumulation in wild type, *fig-1*(Δcoding sequence), and

2 independent lines expressing *fig-1ΔC6* cDNA from the *fig-1* promoter, an AMsh glia-specific promoter (*F16F9.3*), or an amphid neuron-specific promoter (*dyf-11*). *n* (number of trials scored, 20 animals/ trial) indicated inside bars. Adjusted *P* values in relation *to fig-1*(Δcoding sequence) calculated using Tukey's multiple comparison test following one-way ANOVA. **f** Widefield images of a *fig-1::sfGFP* animal expressing AMsh membrane reporter *F16F9.3pro::myr-mKate2*. Arrowheads, anterior FIG-1::sfGFP puncta. Arrows, FIG-1::sfGFP within AMsh glia. Scale bar = 10 μm. **g** Confocal images of *fig-1::sfGFP* animal expressing DGS-1::mKate2. Arrowheads, anterior FIG-1::sfGFP puncta. Arrows, FIG-1::sfGFP around cilia base. Scale bar = 10 μm. Fluorescence images are maximum intensity projections z-stacks. Data are represented as mean + SEM. Source data are provided as a Source Data file.

DGS-1 and FIG-1 function in the glial cilia damage detection pathway and physically interact

To probe the relationship between *dgs-1*, *fig-1*, and dendrite cilia mutants, we examined the DGS-1::mKate2 reporter in cilia and *fig-1*

mutants. Although DGS-1::mKate2 is still transported to cilia-disrupted dendrite tips in *che-2(e1033)* mutants (Fig. 5a), overall expression of this reporter is reduced (Fig. 5a [dotted ellipses], b). This result suggests that activation of the glial response in *che-2(e1033)* mutants may
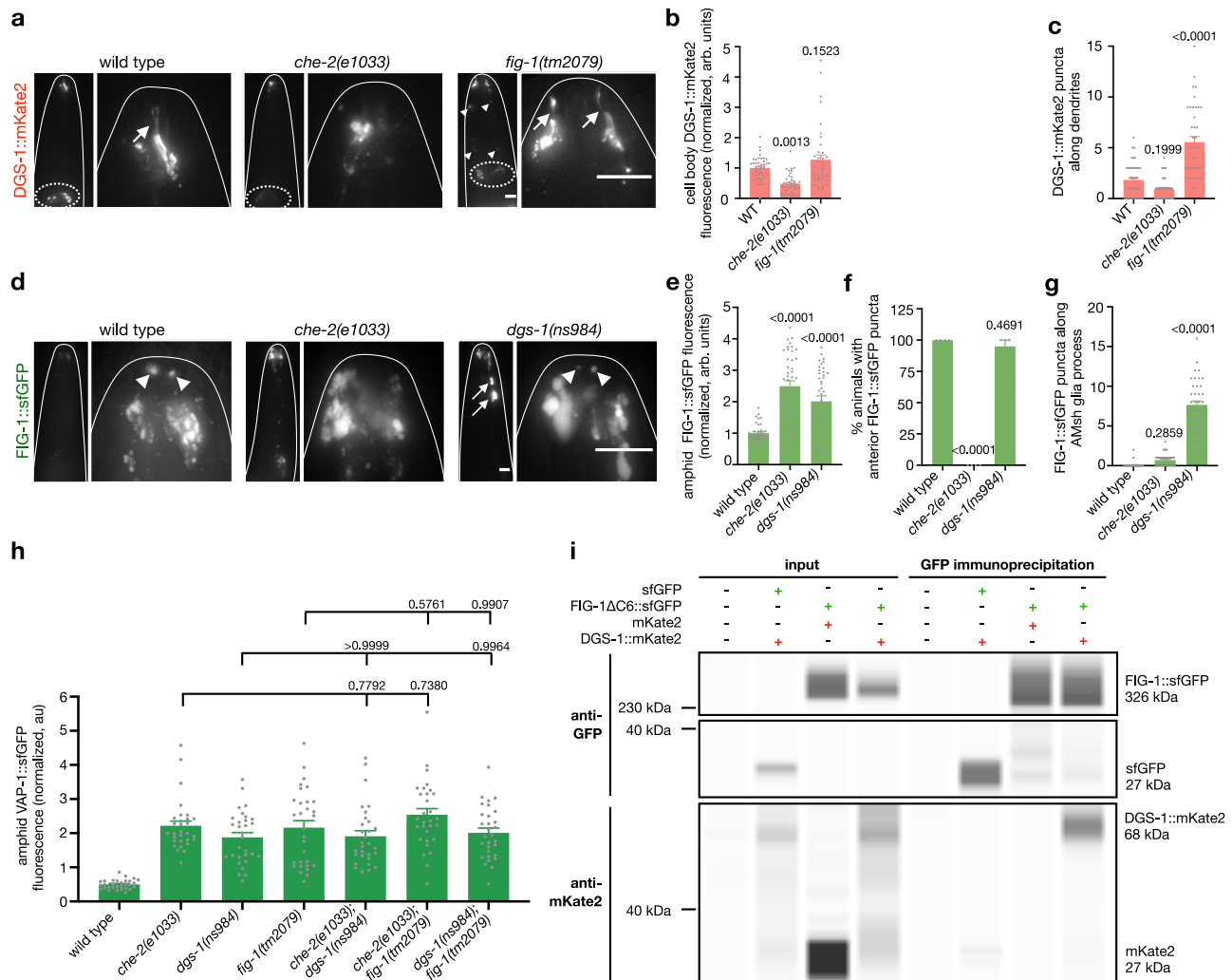
Fig. 5 | DGS-1 and FIG-1 function in the same pathway and physically interact.
a Brightness and contrast-matched images of animals expressing DGS-1::mKate2 in a wild type animal, and *che-2(e1033)* and *fig-1(tm2079)* mutants representative of dataset quantified in **b** and **c**. Left panels, brightness and contrast matched head region. Right panels, nose tip inset. Arrows, dendrite cilia. Arrowheads, DGS-1::mKate2 accumulation along dendrites. Dotted ellipses, neuron cell bodies. Scale bar = 10 μm. **b** Quantification of DGS-1::mKate2 fluorescence in neuron cell bodies. *n* = 40 animals from 4 independent experiments. **c** Quantification of DGS-1::mKate2 puncta along the dendrites (between buccal cavity and cell bodies) per animal. *n* = 40 animals from 4 independent experiments. **d** Images of FIG-1::sfGFP in a wild type animal, and *che-2(e1033)* and *dgs-1(ns984)* mutants representative of dataset quantified in **e–g**. Left, brightness and contrast-matched head images. Right, nose tip inset with brightness and contrast scaled to show FIG-1::sfGFP localization. Arrowheads, anterior FIG-1::sfGFP accumulation. Arrows, FIG-1::sfGFP in ≥2um diameter puncta along the AMsh glial processes. Scale bar = 10 μm.

e Quantification of FIG-1::sfGFP fluorescence in the amphid. *n* = 40 animals from 4 independent experiments. **f** Quantification of percent of animals with at least one anterior FIG-1::sfGFP puncta visible/ image stack. *n* = 40 animals from 4 independent experiments. **g** Quantification of FIG-1::sfGFP puncta ≥2 um diameter along the glial processes per animal, defined as between buccal cavity and cell body. *n* =4 independent experiments, 10 animals/ experiment. **h** VAP-1::sfGFP quantification in the amphids of animals with indicated genotypes. *n* = 30 animals from 3 independent experiments. **i** Co-immunoprecipitation of FIG-1ΔC6::sfGFP or sfGFP from *Drosophila* S2 cells co-transfected with DGS-1::mKate2 or mKate2. Experiment was performed 5 times with similar results. All fluorescence images are maximum intensity projections of widefield z-stacks. Data are represented as mean + SEM. Adjusted *P*-values calculated using Tukey's multiple comparison test following ordinary one-way ANOVA. Statistical significance shown in relation to wild type unless otherwise indicated. Source data are provided as a Source Data file.

be due to a combination of reduced DGS-1 expression and inappropriate DGS-1 localization due to cilia disruption. In *fig-1(tm2079)* mutants, DGS-1::mKate2 levels are not significantly changed and the protein localizes to dendrite cilia (Fig. 5a, c). However, the reporter accumulates abnormally in puncta along the dendrites (Fig. 5a [arrowheads], c), indicating that FIG-1 is required for proper DGS-1 localization.

We also examined the FIG-1::sfGFP reporter in *che-2* and *dgs-1* mutants. We observed a marked increase in FIG-1::sfGFP accumulation at the glial tip in both mutants (Fig. 5d [compare brightness and contrast matched whole head images], e). These findings mirror changes we observe in VAP-1 in these mutants (Figs. 1d–f, 3a, c), supporting the

notion that FIG-1 travels through the same secretory route as VAP-1. While we did not observe an increase in *fig-1* mRNA levels (Supplementary Fig. 6e, f), levels of a *fig-1* transcriptional reporter were increased >2.5 fold in the AMsh glia if *che-2(e1033)* mutants compared to wild type (Fig. 6h). Increased *fig-1* expression in cilia mutants is consistent with the finding that its transcription is PROS-1 induced[23]. In *che-2*, but not *dgs-1*, mutants, we also observed loss of the two anterior FIG-1::sfGFP puncta near amphid dendrite cilia tips (Fig. 5d [arrowheads], f), demonstrating that FIG-1 at this location is not relevant for the glial secretion function. Importantly, just as DGS-1 aberrantly accumulates in puncta along sensory neuron dendrites in *fig-1* mutants, FIG-1 accumulates in puncta along the AMsh glial process
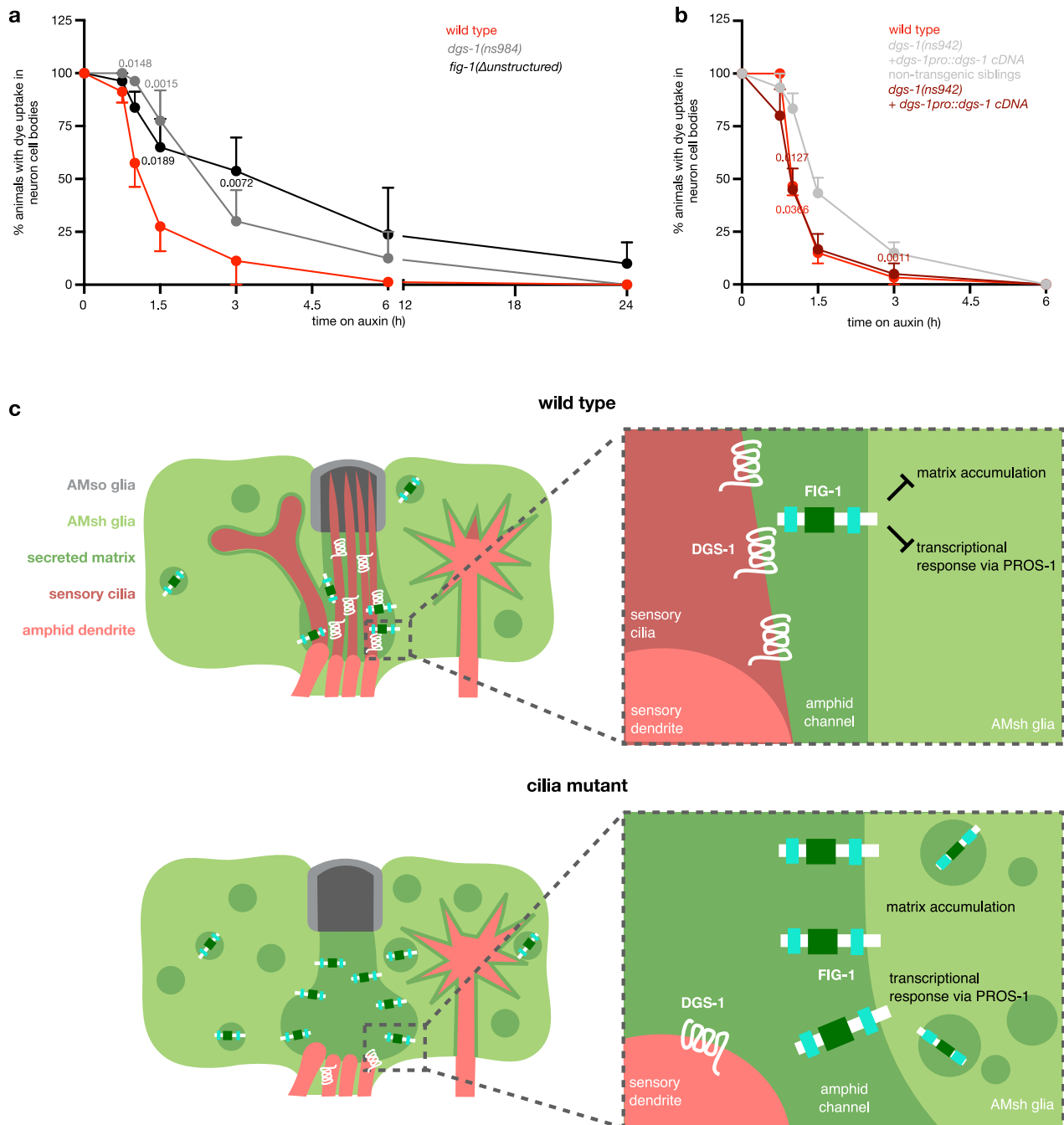
Fig. 6 | The AMsh glial response protects ensheathed dendrite cilia. a, b Dye filling of amphid neuron cell bodies in animals with indicated genotypes also expressing *osm-6::AID*; *eft-3pro::TIR1-mRuby* treated with 400uM auxin for indicated times. Data are represented as mean ± SEM. **a** *n* = 4 trials/ condition, (**b**) *n* = 3 trials/condition with the exception of 3 h auxin treatment +*dgs-1*pro::*dgs-1* cDNA and non-transgenic siblings where *n* = 2 trials/ condition, 20 animals scored/trial; adjusted *P* values calculated using Dunnett's multiple comparison test following 2-way ANOVA, shown in relation to wild type at the same timepoint (**a**), or *dgs-1(ns942); dgs-1pro::dgs-1* cDNA non-transgenic siblings (**b**), only shown if *P* < 0.05. Source data are provided as a Source Data file. **c** Model for AMsh glial detection of and response to loss of ensheathed dendrite cilia.

of *dgs-1* mutants (Fig. 5d [arrows], g). Thus, DGS-1 is reciprocally required for FIG-1 localization.

To test if *dgs-1*, *fig-1*, and cilia genes such as *che-2*, function in the same pathway, we generated animals carrying pair-wise combinations of mutants and assayed activation of the glial response. We found that double-mutant animals accumulate VAP-1::sfGFP in the amphid to the same extent as each single mutant (Fig. 5h). Supporting this, serial-section TEM of *dgs-1(ns984); fig-1(Δcoding sequence)* double mutants does not reveal additional channel or vesicle matrix accumulation

compared to either single mutant (Supplementary Fig. 8, 2 amphids observed; compare to Figs. 3e, 4d). We conclude that double mutants fail to give an enhanced glial response because all three genes function in the same pathway.

We then asked if DGS-1 and FIG-1 physically interact. We co-expressed *fig-1ΔC6*::sfGFP or sfGFP in pairwise combinations with *dgs-1*::mKate2 or mKate2 in *Drosophila* S2 cells and performed anti-GFP immunoprecipitation. DGS-1::mKate2 was immunoprecipitated in cells co-transfected with FIG-1::sfGFP, but not sfGFP alone (Fig. 5i). Further

confirming the specificity of the interaction, mKate was not immuno-precipitated from cells co-transfected with FIG-1::sfGFP. We note that this interaction may be occurring in *cis*, between molecules expressed in the same cells, or in *trans*, between molecules expressed in distinct cells.

In summary, our genetic and protein localization data support the conclusion that cilia genes, *dgs-1*, and *fig-1* function in the same pathway promoting AMsh glia responses to ensheathed dendrite cilia damage and our co-immunoprecipitation assay shows that DGS-1 and FIG-1 physically interact.

The AMsh glial response transiently protects neuronal cilia

Secretion from AMsh glia is required for associated sensory neuron function. For example, knockdown of *pros-1* results in loss of expression of many glial secreted and transmembrane proteins and causes sensory neuron dye uptake defects and behavioral deficits in response to sensory stimuli[23]. Furthermore, blocking AMsh glia secretion results in shortened AFD neuron microvilli in a subset of animals[39]. Given these findings, we wondered whether accumulation of glial extracellular matrix in response to dendrite cilia could protect against acute dendrite cilia perturbation. The studies presented in Fig. 2b, e show that in our inducible cilia disruption system, cilia become largely defective within 1.5 h of treatment with 4 mM auxin. However, the endogenous glial secretion response takes about ~6 h to reach full induction– too late to restore cilia function. We, therefore, sought to examine the effects of auxin-mediated cilia destruction in *dgs-1* and *fig-1* mutants, in which the extracellular space around cilia is preloaded with excess secretory material due to constitutive activation of the glial secretory response. As cilia are rapidly destroyed in animals treated with 4 mM auxin, we used ten-fold lower auxin concentrations in these experiments. Strikingly, we observed that loss of dye uptake following cilia disruption is significantly delayed in both *dgs-1* and *fig-1* mutants in animals treated with 400 uM auxin (Fig. 6a; note that unlike in Fig. 2b, here we specifically scored dye uptake in neuronal cell bodies). While >70% of wild-type animals are dye-filling defective after 1.5 h on auxin, *dgs-1(ns984)* and *fig-1(Δunstructured)* mutants require at least 3 h to manifest a similar defect. Importantly, we observe faster dye filling loss in *dgs-1(ns942)* mutants expressing *dgs-1* cDNA under its endogenous promoter (*dgs-1pro::dgs-1* cDNA) than in non-transgenic siblings (Fig. 6b). While it is possible that mutations in both *dgs-1* and *fig-1* induce secretion-independent changes that extend the duration of dye uptake, we favor the interpretation that the glial responses to cilia disruption elicited by these mutants are protective.

Discussion

We show here that *C. elegans* AMsh glia detect and mount a protective response to defects in dendrite substructure. Our studies also uncover key proteins mediating this glial response. Our findings support a model in which DGS-1, localizing to dendrite cilia, binds to FIG-1 on associated glia to signal the presence of dendrite cilia (Fig. 6c). FIG-1 inhibits AMsh glia matrix accumulation when cilia are intact, ensuring optimal levels and composition of AMsh glia-secreted extracellular matrix around cilia. When cilia are damaged, DGS-1 levels decrease, and the protein is not properly distributed. This attenuates FIG-1 inhibitory activity, resulting in accumulation of glia-secreted matrix and changes in glial transcription, including changes to the panel of membrane and secreted proteins. The effect of this glial response is to protect cilia from damage, although this response cannot protect from complete cilia destruction.

Neuronal DGS-1 binds to glial FIG-1 to signal intact dendrite cilia

Our findings suggest that DGS-1, a 7-transmembrane domain protein, signals the presence of intact dendrite cilia to surrounding AMsh glia. Many 7-transmembrane domain proteins function as G protein-coupled receptors (GPCRs), but DGS-1 does not have sequence homology to characterized *C. elegans* GPCR families, nor does it possess conserved G protein-coupling motifs[40]. Instead, we find here that DGS-1 directly binds to FIG-1, likely serving to signal the presence of associated dendrite cilia to associated glia.

Loss of FIG-1b in AMsh glia triggers the glial response to loss of dendrite cilia. Our structure-function studies show that both intracellular and extracellular domains of FIG-1b are required for its function. Therefore, it is possible that FIG-1b may transmit the signal of intact dendrite cilia structure across the glial membrane to initiate responses, and therefore, may function as a signaling receptor. Alternatively, FIG-1 could serve as a co-receptor for a yet unidentified receptor protein.

Our studies also reveal that FIG-1b has two distinct and separable activities: one in regulating the protective AMsh glial response to cilia disruption and another in promoting neuronal dye uptake[29]. The localization of some FIG-1b protein to two puncta outside of AMsh glia suggests that the protein is cleaved extracellularly. Based on our domain deletion studies, we propose that the intact transmembrane protein may mediate the AMsh glial response, and that a cleaved extracellular fragment may control dye uptake. These results are also supported by cell-specific rescue data: matrix accumulation can only be rescued by expression in AMsh glia, while neuronal dye uptake can be rescued by expression in AMsh glia or amphid neurons[29]. We also find that mutations that affect each of these activities have opposing effects on dye uptake of associated amphid neurons; while we identify loss of function mutants and domain deletions that cause amphid dye filling defects, mutations that only cause secreted matrix accumulation extend the duration of dye uptake upon inducible cilia damage.

Changes in glia-secreted matrix protect associated dendrites

How do the glial responses to dendrite structure defects protect associated dendrites? We propose that changes in the composition and quantity of glial-secreted matrix surrounding the dendrite cilia function to protect dendrite cilia structure and/ or function. Indeed, secreted matrix metalloproteases have been shown to promote ciliogenesis[41] and their mutation causes ciliopathies[42]. Conversely, changes in astrocyte secretion contribute to altered neuronal development in neurodevelopmental disorders[43,44], supporting the idea that glial secretion is an important mode of neuron regulation. Furthermore, expression of mammalian thrombospondin domain-containing proteins, including TSP-1/2 and pleiotrophin, are altered in Downs Syndrome and stroke, and promote synaptic plasticity, proper neuronal morphology, and functional stroke recovery[44–46]. Therefore, the impact of secreted proteins on associated cells can be either positive or negative, depending on context[8]. Elucidating the mechanisms of glial protection of dendrites in the amphid therefore warrants further study.

Extending the paradigm

Assessment of dendrite substructure integrity by glia may be a widespread phenomenon, meriting future studies in other contexts and animals. The overall architecture of sensory organs is conserved among animals[11–13]. The proteins that control cilia assembly, including the IFT complex proteins, are highly conserved[47], as is the transcription factor PROS-1/Prospero/Prox1[23,31–33]. Furthermore, ciliated dendrite endings of sensory neurons resemble dendritic substructures at synapses[48]. Thus, it is possible that the integrity of structures such as dendritic spines, is monitored and regulated by their ensheathing astrocytes.

DGS-1 and FIG-1 are conserved in a subset of nematodes and most, if not all, species that have DGS-1 homologs also have FIG-1b homologs, suggestive of possible co-evolution. High sequence variability in these proteins suggests that identifying direct homologs in non-nematode species may be challenging. Intriguingly, however, a subfamily of mammalian adhesion GPCRs, the brain-specific angiogenesis

inhibitors (BAIs), resemble a fusion of FIG-1 and DGS-1 in domain architecture and topology. BAI proteins are cleaved into extracellular and membrane-bound fragments that resemble FIG-1 and DGS-1, respectively[49]. BAIs are expressed in mammalian neurons and glia and regulate synaptogenesis and dendritic spine formation[49]. Therefore, investigating whether BAIs are functionally analogous to DGS-1 and FIG-1 warrants future study.

Methods

Caenorhabditis elegans strains and handling
Experiments were performed in synchronized populations of one-day-old hermaphrodites, unless otherwise noted. Animals were grown on nematode growth media plates seeded with *E. coli* strain OP50 as a food source, with the exception of animals used for RNA-seq experiments which were grown in liquid culture with *E. coli* strain HB101 as a food source. Strains were maintained using standard methods[50]. *C. elegans* Bristol strain N2 (RRID:WB-STRAIN:WBStrain00000001) was used as wild type. A complete list of strains generated and used in this study is listed in Table S1.

CRISPR/Cas9 genome editing
vap-1(ns831[vap-1::sfGFP]) was generated using plasmid-based methods[51]. Briefly, an sgRNA guide sequence targeting the 3′ end of *vap-1* (5′- gttgcatagaaaatttacta- 3′) was cloned into pDD162, creating plasmid pKV2. A homologous recombination template plasmid, pKV3, was cloned, containing the following elements: (1) 1.5 kb *vap-1* 5′ homology arm of *vap-1* coding sequence, (2) an in frame flexible linker coding for amino acid sequence: PDPRDWPKDRK, (3) an artificial intron containing *unc-119*(+) rescuing sequence in the antisense direction flanked by LoxP sites, (4) additional in frame flexible linker coding for amino acid sequence: EDPWRVP, (4) in frame sfGFP coding sequence, (5) 1.5 kb *vap-1* 3′ homology arm of intergenic sequence, and (6) plasmid backbone from pPD95.75. Note that a silent mutation was introduced in the final codon of the sfGFP sequence to disrupt a potential PAM site immediately following the sgRNA guide target site. pKV2 and pKV3 were injected along with red fluorescent co-injection markers into strain DP38. Progeny were screened for rescue of uncoordinated phenotype without expression of red co-injection markers and genotyped for insertion of desired sequence into the *vap-1* locus. Once insertion of the desired sequence was verified, animals were injected with pPD104 to remove *unc-119*(+) rescuing sequence and backcrossed with N2 to remove the *unc-119(ed3)*III mutation, creating strain OS11927.

dgs-1(ns984) was generated by imprecise insertion via injection of Cas9, tracrRNA, and crRNA (5′- tggaataatgctcggacgtg -3′) from IDT[52]. The following alleles were generated by SUNY biotech:
- *osm-6(syb2906[osm-6*::gfp-aid])V - C-terminal knock-in of coding sequences of: (1) linker sequence: GASGASGAS, (2) GFP, and (3) AID
- *osm-6(syb2906 syb4401[osm-6*::gfp-aid])V - precise deletion of GFP sequence from *osm-6(syb2906)*
- *dgs-1(ns942 syb3113)*IV - precise nucleotide replacement, reverting *dgs-1(ns942[G58 > E])* allele to wild type, E58 > G
- *fig-1(syb6983[fig-1Δcoding sequence])V* - precise deletion of *fig-1* coding sequence
- *fig-1(syb5898[fig-1ΔSS/TMD])V* - precise deletion of *fig-1b* transmembrane domain (FIG-1B amino acids 23-51)
- *fig-1(syb7619[fig-1ΔC-terminus])V* - precise deletion of *fig-1* C-terminus (FIG-1B amino acids 2874–2898)
- *fig-1(syb7600[fig-1ΔN-terminus])V* - precise deletion of *fig-1b* N-terminus (FIG-1B amino acids 2-22)
- *fig-1(syb7606[fig-1Δunstructured])V* - precise deletion of *fig-1b* unstructured extracellular region (FIG-1B amino acids 115−754)
- *fig-1(syb6326[fig-1Δtsp C])V* - precise deletion of *fig-1* C-terminal thrombospondin type 1 repeat (FIG-1B amino acids 2823–2873)

- *fig-1(syb6326 syb6968[fig-1Δtsp N + tsp C])V* - precise deletion of *fig-1* N-terminal and C-terminal thrombospondin type 1 repeats (FIG-1B amino acids 62–114 & 2823–2873)
- *fig-1(syb7051[fig-1Δisoform a])V* - precise deletion of *fig-1b* intron 19 containing the first exon of *fig-1a*
- *fig-1(syb5954[fig-1Δtsp N])V* - precise deletion of *fig-1b* N-terminal thrombospondin type 1 repeat (FIG-1B amino acids 62-114)
- *fig-1(syb6039[fig-1ΔC6])V* - precise deletion of *fig-1b* region containing 17 C6 repeats (FIG-1B amino acids 755−2788)
- *fig-1(syb7231[fig-1*::sfGFP C-terminal])V - C-terminal knock-in of coding sequences for: (1) flexible linker with amino acid sequence: PDPRDWPKDPK (2) sfGFP
- *fig-1(syb7028[fig-1*::sfGFP internal])V- knock-in of coding sequences for the following after FIG-1B amino acid 754: (1) flexible linker with amino acid sequence: PDPRDWPKDPK, (2) sfGFP, (3) flexible linker with amino acid sequence: GGSGGGSGGGSG
- *fig-1(syb8275 [fig-1Δunstructured])V* – recreation of precise deletion of *fig-1b* unstructured extracellular region (FIG-1B amino acids 115-754) in *osm-6(syb2906 syb4401)* background

Generation of recombinant DNA via PCR fusion
Several fluorescent reporters and rescuing DNA sequences were generated using a PCR fusion approach[53]. First, two fragments were amplified via PCR: (1) promoter sequences containing 24−29 bp of homology region to the 5′ sequence of fragment 2, added via the reverse PCR primer, and (2) coding sequence of fluorescent report or rescuing cDNA and UTRs. The two fragments were then fused via PCR and amplified using internal nested primers. *F16F9.3*pro::myr-mKate2 was created by fusing: (1) 2056 bp *F16F9.3* promoter region and (2) coding sequence for myr-mKate2 followed by the *unc-54* 3′ UTR. *C01B10.7*pro::GFP, *T10H4.13*pro::GFP, *srr-1*pro::GFP, *F57E7.4*pro::GFP, and *dgs-1*pro::GFP were created fusing: (1) 560, 1185, 2555, 586, or 2985 bp intergenic regions upstream of relevant genes, respectively, and (2) GFP followed by the *unc-54* 3′UTR. *dgs-1*pro::dgs-1 cDNA was created by fusing: (1) 2985 bp intergenic region upstream of *dgs-1* and (2) *dgs-1* cDNA with endogenous 5′ and 3′ UTRs. *dyf-11*pro::dgs-1 cDNA was created by fusing: (1) a 1864 bp *dyf-11*pro and (2) *dgs-1* cDNA with endogenous 5′ and 3′ UTRs. A complete list of oligonucleotides used in the study is listed in Table S2.

Plasmid construction
Plasmids were constructed using Gibson cloning.

Cell-specific TIR1-mRuby plasmids were created by subcloning TIR1-mRuby followed by the *unc-54* 3′UTR amplified from pLZ31[34] (fragment) into plasmids containing the following cell-specific promoters (vectors): (1) a 1864 bp *dyf-11*pro (pKV13), (2) a 2056 bp *F16F9.3*pro (pKV14), (3) a 3.2 kb *srh-142*pro (pKV16) (4) a 1.0 kb *srg-47*pro (pKV17), (4) a 2985 bp *dgs-1*pro (pKV15). DGS-1::mKate2 (pKV12) was created by Gibson assembly of 3 fragments: (1) a vector containing the 2985 bp *dgs-1* promoter, endogenous 5′ UTR, and *dgs-1* cDNA to the center of the 3rd intracellular domain (amino acids 1-239), (2) mKate2 flanked by flexible linkers (PDPRDWPKDPK/ GGSGGGSGGGSG), and (3) the remaining *dgs-1* cDNA (amino acids 240-stop) followed by the endogenous 3′UTR. *fig-1*pro::fig-1ΔC6 cDNA (pKV34) was created by inserting *fig-1*b cDNA in two fragments (1) amino acids 1-754 and (2) amino acids 2,789-stop into a vector containing a 1872 bp *fig-1* promoter. *F16F9.3*pro:: fig-1ΔC6 cDNA (pKV35) and *dyf-11*pro:: fig-1ΔC6 cDNA (pKV36) were generated by replacing the *fig-1*pro in pKV34 with: (1) a 2056 bp *F16F9.3* or (2) 1864 bp *dyf-11* promoter, respectively. *Drosophila* S2 cell expression constructs were created by subcloning (1) *sfGFP* (pKV40), (2) mKate2 (pKV41), (3) *fig-1(ΔC6)*::sfGFP (pKV42), and (4) *dgs-1*::mKate2 (pKV43) coding sequences into a vector containing the *Drosophila melanogaster* actin promoter and SV40 polyA sequences amplified from pXD49. Note that mKate2 was reassembled to remove

introns via PCR fusion. A complete list of oligonucleotides used in the study is listed in Table S2.

Germline transformation and integration

Plasmid mixes containing the plasmid(s) of interest, co-injection markers, and pBluescript were injected into the gonads of young adult hermaphrodites at a total of 100 ng/ul. Injected animals were singled onto NGM plates and allowed to grow for one generation. Transformed animals were screened for the expression of fluorescent co-injection markers, singled, and screened for stable inheritance of the extrachromosomal array. Only distinct F1s or lines from different P0 injected hermaphrodites were considered independent.

Integrated transgenic constructs (nsIs971 and nsIs972) were generated by exposure to 33.4 μg/mL trioxsalen and UV irradiation using a Stratagene Stratalinker UV 2400 Crosslinker (360 μJ/cm2 x100)[54].

Microscopy

Animals were anesthetized using 50 mM NaN_3 and mounted on 2% agarose pads on glass slides. Widefield z-stacks (0.3–1 μm thick) were taken using a Zeiss compound microscope (Axio Imager M2) using a 63X objective controlled by MicroManager software (v1.4.22)[55]. Confocal z-stacks (0.3–1 μm thick) were taken using a Zeiss LSM900 using a 63X objective controlled by ZenBlue software. ImageJ software was used to produce maximum projections of z-stack images.

VAP-1::sfGFP accumulation scoring

Animals were anesthetized on ice for -10–60 min prior to observation with a fluorescence dissecting microscope equipped with a 2X objective (Leica). Animals with obvious GFP accumulation at the nose tip were scored as strong, animals in which it was unclear if GFP accumulation was in excess of wild type were scored as weak, and animals with no visible GFP fluorescence were scored as none.

Cell isolation and FACS analysis

-2 million synchronized larvae expressing F16F9.3pro::dsRed in wild type or che-2(e1033) background (OS4079 and OS11549) were grown from L1 arrest in S-basal liquid culture containing E. coli HB101 at 20 °C, shaking. After 36–42 h, late-stage larvae (L3 and L4) were pelleted by centrifugation (2 min, 210xg) and subsequently washed ten times with M9 to remove excess bacteria. Each wash consisted of a brief (10 s, $210 \times g$) centrifugation, such that most animals were pelleted, but bacteria remained in suspension. Animals were then dissociated using SDS-DTT (0.25% SDS; 200 mM DTT; 20 mM HEPES, pH 8.0; 3% sucrose) and Pronase E (15 mg/ml)[56]. SDS-DTT was added at a 2:1 ratio the volume of packed animal pellet, followed by 4 min incubation on ice. After washing, 4:1 ratio of Pronase E was added to the packed animal pellet and animals were incubated rotating at 20 °C for 5 min, followed by 12 min of gentle homogenization (2 mL dounce homogenizer, pestle clearance 0.0005-0.0025 inches). After washes with ice-cold egg buffer (1.18 M NaCl; 480 mM KCl; 20 mM $CaCl_2$; 20 mM $MgCl_2$; 250 mM HEPES, pH 7.3) to remove Pronase E, cells were filtered through a 5 μM filter to remove undigested animal fragments, and immediately sorted by FACS.

AMsh glia cell sorting was performed using a BD FACS Aria sorter equipped with a 561 nm laser (Rockefeller University Flow Cytometry Resource Center), with egg buffer as the sheath buffer to preserve cell viability. Dead cell exclusion was carried out using DAPI, while DRAQ5 was used to distinguish nucleated cells from non-nucleated cell fragments. Gates for size and granularity were adjusted to exclude cell aggregates and debris. Gates for fluorescence were established using wild type non-fluorescent animals. Additional information on flow cytometry gating strategy is provided in Supplementary Information. 168,356–240,125 dsRed-positive events were sorted per replicate, which represented 0.1–0.4% of total events (after scatter exclusion), which is roughly the expected labeled-cell

frequency in the animal (-0.21%). dsRed-negative events from the same gates of size and granularity, representing all other cell types, were also sorted for comparison. Cells were sorted directly into TRIzol LS at a ratio 3:1 (TRIzol to cell volume).

RNA isolation and sequencing

RNA was extracted from Trizol LS-treated cells by phase separation, following the manufacturers guidelines. RNA was purified using Pico-Pure RNA isolation kit. 0.4–5 ng purified total RNA was obtained per sample. All subsequent steps were performed by the Rockefeller University Genomics Resource Center. RNA quality was verified using an Agilent Bioanalyzer to ensure sample degradation had not occurred. mRNA amplification and cDNA preparation were performed using the SMARTer mRNA amplification kit. Labeled samples were sequenced using an Illumina HiSeq 2000 sequencer and standard Illumina sequencing primers.

RNA-seq quality assessment

Fastq files were generated with CASAVA v1.8.2, and examined using FASTQC for sequence quality. Reads were aligned to C. elegans WS262 genome release (https://downloads.wormbase.org/releases/WS262/species/c_elegans/PRJNA13758/) using the STAR v2.3 aligner with parameters (--out- Filter Multi map Nmax 10 --outFilterMultimapScoreRange 1). The alignment results were evaluated using RNA-SeQC v1.17 to make sure all samples had a consistent alignment rate and no obvious 5' or 3' bias. Aligned reads were summarized through featureCounts with gene models from Ensemble (Caenorhabditis_elegans. WBcel235.77.gtf) at gene level unstranded. Specifically, the uniquely mapped reads (NH "tag" in bam file) that overlapped with an exon (feature) by at least 1 bp on either strand were counted and then the counts of all exons annotated to an Ensemble gene (meta features) were summed into a single number. rRNA genes, mitochondrial genes and genes with length <40 bp were excluded from downstream analysis.

RNA-seq differential gene expression analysis

Experiments were performed with 3 independent replicates. DESeq2 was applied to normalize count matrix and to perform differential gene-expression analysis, comparing: (1) RNA counts derived from the AMsh glia cells (dsRed positive) to RNA counts that were derived from all other C. elegans cells (dsRed negative) from both wild type and cilia mutant [che-2(e1033)], and (2) AMsh glia from wild type to AMsh glia from cilia mutant, using negative binomial distribution[57]. To identify transcripts up- or down- regulated in cilia mutant compared to wild type AMsh glia, we used a fold-change cut offs of >2 and <0.5, respectively, and an adjusted p-value threshold of <0.1.

qPCR

RNA from wild type (OS11927) and che-2(e1033) mutants (OS12195) was extracted using Trizol reagent and collected using RNeasy Mini Columns (Qiagen). SuperScript III First-Strand Synthesis System (ThermoFisher Scientific) was used to create cDNA libraries. Digital PCR was performed using PowerUp SYBR Green Master Mix (ThermoFisher) on QuantStudio 3D digital PCR platform (ThermoFisher Scientific) and analyzed using QuantStudio v1.5.3 software and ΔCt analysis.

Inducible cilia disruption

Exposure of C. elegans to the synthetic auxin analog K-NAA (1-napthaleneacetic Acid Potassium Salt), results in ubiquitination and subsequent proteasomal degradation of auxin inducible degron (AID)-tagged proteins in the presence of transgenically provided TIR1, the substrate recognition component of the E3 ubiquitin ligase complex[34,58]. Strains carrying osm-6::gfp::aid [osm-6(syb2906)] or osm-6::aid (osm-6(syb2906 syb4401) were crossed with a strain ubiquitously expressing TIR1 tagged with mRuby (ieSi57 [eft-3pro::TIR1-mRuby]) or injected with constructs expressing TIR1-mRuby under cell specific

promoters. K-NAA was dissolved in sterile water to prepare a 200 mM stock solution for 4 mM auxin treatment or 20 mM stock solution for 400 uM auxin treatment. For 72 h auxin treatment, OP50-seeded NGM plates were pre-coated with K-NAA to a final concentration of 4 mM and synchronized populations of animals were transferred to K-NAA plates. For all other timepoints, K-NAA was added to the desired concentration directly to animals on seeded plates and allowed to dry before the remaining incubation.

Neuronal Dye Filling

5 mg/mL DiI (1,1'-dioctadecyl-3,3,3'3'-tetramethylindocarbocyanine perchlorate) and 2 mg/mL DiO (3,3'-Dioctadecyloxacarbocyanine perchlorate) stock solutions were made in N,N-dimethylformamide. Animals were incubated with dye solution, diluted in M9 to a final concentration of 5 µg/ml for DiI or 8 µg/mL for DiO, for (1) 15–60 min for routine dye filling assays or (2) 5 min for dye filling time course experiments. Animals were then washed twice in M9, and transferred to seeded plates at least 10 min to remove excess dye prior to scoring. Dye filling was scored as complete, partial, or none, as compared to wild type using fluorescence dissecting microscopes. For experiments in Fig. 6a, b, animals were anesthetized on ice for ~10–60 min prior to scoring and dye filling was scored as positive or negative in the cell bodies of neurons.

Mutagenesis and mutant identification

OS12214 animals were mutagenized using 75 mM ethylmethanesulfonate for 4 h at 20 °C. ~10,000 F2 progeny were screened for VAP-1::sfGFP accumulation and animals with strong accumulation were transferred to individual plates. A secondary screen was performed to exclude isolates with neuronal dye filling defects, indicating defects in dendrite cilia.

SNP mapping

ns942 mutants were crossed to CB4856 Hawaiian males. F2 animals with VAP-1::sfGFP accumulation were isolated, and progeny were lysed and genotyped for 3 SNPs between N2 and Hawaiian backgrounds on each chromosome. Additional SNPs were used to map *ns942* to a ~ 4.5 map unit segment of chromosome IV.

Whole genome sequencing

ns942 and parental OS12214 animals were grown on *E. coli* strain OP50 until bacteria were depleted, harvested in M9, and resuspended in 0.5 mL TEN buffer (20 mm Tris pH 7.5, 0.5 M EDTA, 100 mM NaCl), pH 7.5. SDS (0.5%), proteinase K (0.1 mg/mL), and β-mercaptoethanol (0.2%) were added. The lysis reaction was incubated overnight in a shaking thermocycler at 56 °C. Phenol/chloroform was added and phase-separated by spinning in a phase-lock tube. The aqueous phase was transferred to 200 proof EtOH. The resulting DNA clot was washed in 70% EtOH, dried, and resuspended in TEN. After rehydration, 0.3 µL of 100 mg/mL RNAse A was added and incubated at 37 °C for 2 h. Phenol/chloroform extraction was performed again and DNA was rehydrated with EB buffer. The sample was then examined using a nanodrop spectrophotometer and run on a 1% agarose gel to confirm that there was no RNA contamination or DNA degradation, respectively. NextSeq Mid Output 2 × 150 sequencing was performed using Standard Illumina Sequencing primers for gDNA-seq application.

Electron microscopy

Synchronized young adult animals were fixed, stained, embedded in resin, and sectioned using standard methods[59]. For OSM-6::AID; *eft-3*pro::TIR1-mRuby; *vap-1(ns831)* animals treated with auxin for 3 h, after 1.5 h of auxin treatment, an abbreviated dye filling assay was performed in the presence of 4mM K-NAA, and dye filling defective animals were selected for imaging after 3 h auxin treatment total. Serial images were acquired by using a Titan Themis 200 kV transmission electron microscope with Cs Image Corrector. Image processing and analysis were performed using ImageJ and IMOD software.

Percent conservation and amino acid alignment

Amino acid sequences of DGS-1 and FIG-1b from *C. elegans* and homologous proteins in additional *Caenorhabditis* species were compared using NCBI blastp suite. Percent conservation was calculated by multiplying % query coverage by % identities. Sequence alignment was created using Jalview following multiple sequence alignment from Muscle (EMBL-EBI).

Drosophila S2 Cell Culture and co-immunoprecipitation assays

Drosophila S2 Cells were cultured in Schneider's *Drosophila* Medium supplemented with 10% fetal bovine serum at 27 C. 10 cm dishes of cells were transfected using Qiagen Effectene according to manufacturer's instructions.

Three days after transfection, cells were treated with 10uM MG-132 for 2–3 h, washed with PBS, pelleted, and frozen at −80C. Cell pellets were thawed in lysis buffer (50 mM Tris pH8, 150 mM NaCal, 1% IPGAL CA-630, 10% glycerol, 10uM MG-132, 1X protease inhibitors) for 30 min and centrifuged to remove the insoluble fraction. Protein concentration for each lysate was determined using BCA Protein Quantification. Equal protein quantities for each lysate were added to GFP-Trap Magnetic Particles (ChromoTek M-270) pre-blocked with 4% BSA and rotated at 4 C for 1 h. Magnetic particles were washed 3 times with TBST and bound proteins were eluted in immunoprecipitation buffer (50 mM Tris pH8, 150 mM NaCl, 10% glycerol, 2% SDS, 25 mM DTT, 35 mM B-ME, 1X protease inhibitors) by boiling at 95 C for 5 min. Proteins from lysate (equal protein quantities) and immunoprecipitation (equal volumes) samples were detected using Simple Western Automated Western Blot System (Wes, Bio-Techne) with rabbit anti-pan RFP (1:100 ChromoTek pabr1 polyclonal Lot #D0000170) or rabbit anti-GFP (1:400 proteintech 50430-2-AP polyclonal Lot #00143536) and analyzed using Compass for Wimple Western Software v6.1.0.

Quantification and statistical analysis

All fluorescence microscopy quantifications were performed in ImageJ v1.5 s[60]. Control and experimental animals imaged during the same imaging session with all acquisition parameters maintained constant between the conditions. For quantification of VAP-1::sfGFP amphid fluorescence, a trapezoidal region of interest (ROI) was drawn in the DIC channel, with the nose tip as the anterior boundary and the buccal cavity as the posterior boundary and fluorescence was measured in a sum z-projection. For quantification of cell body fluorescence, a rectangular ROI was drawn around the diameter of the animal where cell body fluorescence was observed fluorescence was measured in a sum z-projection. For quantification of puncta/ animal, puncta were followed and counted through z-stacks through entire worm, comparing to relevant ROI for size comparison as noted. For quantification of transcriptional reporter fluorescence in AMsh glia, AMsh glia were identified by their proximity to the terminal pharyngeal bulb and the presence of *mir-228pro::nlsRFP* positive nuclei, circular ROIs were drawn around the AMsh nucleus a single z slice in which the nucleus was most in focus, and a cytoplasmic region within AMsh glia one ROI diameter away from the nucleus was quantified. Mean, background subtracted fluorescence is reported. If normalized, the mean of the wild type condition for each experimental imaging session was used for normalization.

Prism software (v9) was used for statistical analysis, with statistical tests noted in Figure Legends. For gene list overlap statistics, normal approximation to the hypergeometric probability was calculated (http://nemates.org/MA/progs/overlap_stats.html; Jim Lund, personal communication).

Reporting summary

Further information on research design is available in the Nature Portfolio Reporting Summary linked to this article.

Data availability

All reagents are available from the corresponding author upon request. The raw and processed RNA-seq data generated in this study have been deposited have been deposited in the Gene Expression Omnibus under accession code GSE282640. The whole genome sequencing data generated in this study have been deposited in the NCBI Sequence Read Archive under accession code PRJNA1189083 [https://www.ncbi.nlm.nih.gov/sra/SRX26803813, https://www.ncbi.nlm.nih.gov/sra/SRX26803814]. Source data are provided with this paper.

References

1. Bentley, M. & Banker, G. The cellular mechanisms that maintain neuronal polarity. *Nat. Rev. Neurosci.* **17**, 611–622 (2016).
2. Nave, K. A. & Werner, H. B. Myelination of the nervous system: mechanisms and functions. in *Annual Review of Cell and Developmental Biology* Vol. 30, 503–533 (Annual Reviews, 2014).
3. Nimchinsky, E. A., Sabatini, B. L. & Svoboda, K. Structure and function of dendritic spines. *Annu. Rev. Physiol.* **64**, 313–353 (2002).
4. Allen, N. J. & Eroglu, C. Cell biology of astrocyte-synapse interactions. *Neuron* **96**, 697–708 (2017).
5. Sengupta, P. Cilia and sensory signaling: the journey from 'animalcules' to human disease. *PLoS Biol.* **15**, e2002240 (2017).
6. Barres, B. A. The mystery and magic of glia: a perspective on their roles in health and disease. *Neuron* **60**, 430–440 (2008).
7. Michailov, G. V. et al. Axonal neuregulin-1 regulates myelin sheath thickness. *Science (1979)* **304**, 700–703 (2004).
8. BrosiusLutz, A. & Barres, B. A. Contrasting the glial response to axon injury in the central and peripheral nervous systems. *Dev. Cell* **28**, 7–17 (2014).
9. Runge, K., Cardoso, C. & de Chevigny, A. Dendritic spine plasticity: function and mechanisms. *Front. Synaptic Neurosci.* **12**, 36 (2020).
10. Waters, A. M. & Beales, P. L. Ciliopathies: an expanding disease spectrum. *Pediatr. Nephrol.* **26**, 1039–1056 (2011).
11. Shanbhag, S. R., Müller, B. & Steinbrecht, R. A. Atlas of olfactory organs of Drosophila melanogaster 2. Internal organization and cellular architecture of olfactory sensilla. *Arthropod Struct. Dev.* **29**, 211–229 (2000).
12. Prelic, S. et al. Functional interaction between drosophila olfactory sensory neurons and their support cells. *Front Cell Neurosci* **15**, 789086 (2022).
13. Getchell, M. L. & Getchell, T. V. Fine structural aspects of secretion and extrinsic innervation in the olfactory mucosa. *Microsc. Res. Tech.* **23**, 111–127 (1992).
14. Singhvi, A. & Shaham, S. Glia-neuron interactions in caenorhabditis elegans. *Annu. Rev. Neurosci.* **42**, 149–168 (2019).
15. Ward, S., Thomson, N., White, J. G. & Brenner, S. Electron microscopical reconstruction of the anterior sensory anatomy of the nematode caenorhabditis elegans. *J. Comp. Neurol.* **160**, 313–337 (1975).
16. White, J. G., Southgate, E., Thomson, J. N. & Brenner, S. The structure of the ventral nerve cord of Caenorhabditis elegans. *Philos. Trans. R. Soc. Lond. B Biol. Sci.* **275**, 327–348 (1976).
17. White, J. G., Southgate, E., Thomson, J. N. & Brenner, S. The structure of the nervous system of the nematode Caenorhabditis elegans. *Philos. Trans. R. Soc. Lond. B Biol. Sci.* **314**, 1–340 (1986).
18. Inglis, P. N., Ou, G., Leroux, M. R. & Scholey, J. M. The sensory cilia of Caenorhabditis elegans. *WormBook* 1–22 https://doi.org/10.1895/wormbook.1.126.2 (2007).
19. Bargmann, C. I. Chemosensation in C. elegans. *WormBook* 1–29 https://doi.org/10.1895/wormbook.1.123.1 (2006).
20. Shaham, S. Glia-neuron interactions in the nervous system of Caenorhabditis elegans. *Curr. Opin. Neurobiol.* **16**, 522–528 (2006).
21. Doroquez, D. B., Berciu, C., Anderson, J. R., Sengupta, P. & Nicastro, D. A high-resolution morphological and ultrastructural map of anterior sensory cilia and glia in Caenorhabditis elegans. *Elife* **3**, e01948 (2014).
22. Perkins, L. A., Hedgecock, E. M., Thomson, J. N. & Culotti, J. G. Mutant sensory cilia in the nematode Caenorhabditis elegans. *Dev. Biol.* **117**, 456–487 (1986).
23. Wallace, S. W., Singhvi, A., Liang, Y., Lu, Y. & Shaham, S. PROS-1/Prospero is a major regulator of the glia-specific secretome controlling sensory-neuron shape and function in C. elegans. *Cell Rep.* **15**, 550–562 (2016).
24. Perens, E. A. & Shaham, S. C. elegans daf-6 encodes a patched-related protein required for lumen formation. *Dev. Cell* **8**, 893–906 (2005).
25. Fujiwara, M., Ishihara, T. & Katsura, I. A novel WD40 protein, CHE-2, acts cell-autonomously in the formation of C. elegans sensory cilia. *Development* **126**, 4839–4848 (1999).
26. Collet, J., Spike, C. A., Lundquist, E. A., Shaw, J. E. & Herman, R. K. Analysis of osm-6, a gene that affects sensory cilium structure and sensory neuron function in caenorhabditis elegans. *Genetics* **148**, 187–200 (1998).
27. Deane, J. A., Cole, D. G., Seeley, E. S., Diener, D. R. & Rosenbaum, J. L. Localization of intraflagellar transport protein IFT52 identifies basal body transitional fibers as the docking site for IFT particles. *Curr. Biol.* **11**, 1586–1590 (2001).
28. Lewis, J. A. & Hodgkin, J. A. Specific neuroanatomical changes in chemosensory mutants of the nematode Caenorhabditis elegans. *J. Comp. Neurol.* **172**, 489–510 (1977).
29. Bacaj, T., Tevlin, M., Lu, Y. & Shaham, S. Glia are essential for sensory organ function in C. elegans. *Science (1979)* **322**, 744–747 (2008).
30. Kage-Nakadai, E. et al. Caenorhabditis elegans homologue of Prox1/Prospero is expressed in the glia and is required for sensory behavior and cold tolerance. *Genes Cells* **21**, 936–948 (2016).
31. Manning, L. & Doe, C. Q. Prospero distinguishes sibling cell fate without asymmetric localization in the Drosophila adult external sense organ lineage. *Development* **126**, 2063–2071 (1999).
32. Pistocchi, A. et al. The zebrafish prospero homolog prox1 is required for mechanosensory hair cell differentiation and functionality in the lateral line. *BMC Dev. Biol.* **9**, 1–10 (2009).
33. Bermingham-McDonogh, O. et al. Expression of Prox1 during mouse cochlear development. *J. Comp. Neurol.* **496**, 172–186 (2006).
34. Zhang, L., Ward, J. D., Cheng, Z. & Dernburg, A. F. The auxin-inducible degradation (AID) system enables versatile conditional protein depletion in C. elegans. *Development* **142**, 4374–4384 (2015).
35. Nishimura, K., Fukagawa, T., Takisawa, H., Kakimoto, T. & Kanemaki, M. An auxin-based degron system for the rapid depletion of proteins in nonplant cells. *Nat. Methods* **6**, 917–922 (2009).
36. Valperga, G. & de Bono, M. Impairing one sensory modality enhances another by reconfiguring peptidergic signalling in Caenorhabditis elegans. *Elife* **11**, e68040 (2022).
37. Taylor, S. R. et al. Molecular topography of an entire nervous system. *Cell* **184**, 4329–4347.e23 (2021).
38. Christopherson, K. S. et al. Thrombospondins are astrocyte-secreted proteins that promote CNS synaptogenesis. *Cell* **120**, 421–433 (2005).
39. Singhvi, A. et al. A Glial K/Cl transporter controls neuronal receptive ending shape by chloride inhibition of an rGC. *Cell* **165**, 936–948 (2016).
40. Weis, W. I. & Kobilka, B. K. The molecular basis of G protein–coupled receptor activation. *Annu. Rev. Biochem* **87**, 897 (2018).

41. Nandadasa, S. et al. Secreted metalloproteases ADAMTS9 and ADAMTS20 have a non-canonical role in ciliary vesicle growth during ciliogenesis. *Nat. Commun.* **10**, 953 (2019).

42. Choi, Y. J. et al. Mutations of ADAMTS9 cause nephronphthisis-related ciliopathy. *Am. J. Hum. Genet* **104**, 45–54 (2019).

43. Caldwell, A. L. M. et al. Aberrant astrocyte protein secretion contributes to altered neuronal development in multiple models of neurodevelopmental disorders. *Nat. Neurosci.* **25**, 1163 (2022).

44. Brandebura, A. N., Asbell, Q. N., Kristine, M., Micael, B. & Allen, N. J. Dysregulation of astrocyte-secreted pleiotrophin contributes to neuronal structural and functional deficits in Down Syndrome. *bioRxiv* 2023.09.26.559633 https://doi.org/10.1101/2023.09.26.559633 (2023).

45. Liauw, J. et al. Thrombospondins 1 and 2 are necessary for synaptic plasticity and functional recovery after stroke. *J. Cereb. Blood Flow. Metab.* **28**, 1722–1732 (2008).

46. Wang, X. Pleiotrophin: activity and mechanism. *Adv. Clin. Chem.* **98**, 51 (2020).

47. Ishikawa, H. & Marshall, W. F. Ciliogenesis: building the cell's antenna. *Nat. Rev. Mol. Cell Biol.* **12**, 222–234 (2011).

48. Shaham, S. Chemosensory organs as models of neuronal synapses. *Nat. Rev. Neurosci.* **11**, 212 (2010).

49. Stephenson, J. R., Purcell, R. H. & Hall, R. A. The BAI subfamily of adhesion GPCRs: synaptic regulation and beyond. *Trends Pharm. Sci.* **35**, 208–215 (2014).

50. Brenner, S. The genetics of Caenorhabditis elegans. *Genetics* **77**, 71–94 (1974).

51. Dickinson, D. J., Ward, J. D., Reiner, D. J. & Goldstein, B. Engineering the Caenorhabditis elegans genome using Cas9-triggered homologous recombination. *Nat. Methods* **10**, 1028–1034 (2013).

52. Dokshin, G. A., Ghanta, K. S., Piscopo, K. M. & Mello, C. C. Caenorhabditis elegans. *Genetics* **210**, 781–787 (2018).

53. Hobert, O. PCR fusion-based approach to create reporter gene constructs for expression analysis in transgenic C. elegans. *Biotechniques* **32**, 728–730 (2018).

54. Kage-Nakadai, E., Imae, R., Yoshina, S. & Mitani, S. Methods for single/low-copy integration by ultraviolet and trimethylpsoralen treatment in Caenorhabditis elegans. *Methods* **68**, 397–402 (2014).

55. Edelstein, A., Amodaj, N., Hoover, K., Vale, R. & Stuurman, N. Computer control of microscopes using µManager. *Curr. Protoc. Mol. Biol.* Chapter 14, https://doi.org/10.1002/0471142727.mb1420s92 (2010).

56. Katz, M. et al. Glutamate spillover in C. elegans triggers repetitive behavior through presynaptic activation of MGL-2/mGluR5. *Nat. Commun.* **10**, 1–13 (2019).

57. Love, M. I., Huber, W. & Anders, S. Moderated estimation of fold change and dispersion for RNA-seq data with DESeq2. *Genome Biol.* **15**, 550 (2014).

58. Martinez, M. A. Q. et al. Rapid degradation of caenorhabditis elegans proteins at single-cell resolution with a synthetic auxin. *G3: Genes|Genomes|Genet.* **10**, 267 (2020).

59. Lundquist, E. A. et al. elegans Rac proteins and several alternative Rac regulators control axon guidance, cell migration and apoptotic cell phagocytosis. *Development* **128**, 4475–4488 (2001).

60. Schneider, C. A., Rasband, W. S. & Eliceiri, K. W. NIH Image to ImageJ: 25 years of image analysis. *Nat. Methods* **9**, 671–675 (2012).

Acknowledgements

Author contributions

Conceptualization, K.C.V. and S.S.; methodology, K.C.V., B.M.H., L.L., A.F., and S.S.; software, Y. Liang; formal analysis, K.C.V., Y. Liang; investigation, K.C.V., B.M.H., L.L., A,F., and Y. Lu; writing–original draft, K.C.V. writing–review & editing, K.C.V., B.M.H., L.L., A.F., and S.S.; funding acquisition, K.C.V. and S.S.

Competing interests

The authors declare no competing interests.

Additional information

Supplementary information The online version contains supplementary material available at https://doi.org/10.1038/s41467-024-55674-0.

Correspondence and requests for materials should be addressed to Shai Shaham.

Peer review information *Nature Communications* thanks the anonymous reviewers for their contribution to the peer review of this work. A peer review file is available.

Reprints and permissions information is available at http://www.nature.com/reprints

Publisher's note Springer Nature remains neutral with regard to jurisdictional claims in published maps and institutional affiliations.